This article has been accepted for publication in a future issue of this journal, but has not been fully edited. Content may change prior to final publication. Citation information: DOI 10.1109/TAES.2020.3026844, IEEE Transactions on Aerospace and Electronic Systems

Long Coherent Integration in Passive Radar Systems Using Super-Resolution Sparse Bayesian Learning

Alexandra Filip-Dhaubhadel and Dmitriy Shutin
German Aerospace Center (DLR), 82234 Weßling, Germany
Emails: {alexandra.filip and dmitriy.shutin}@dlr.de

***Abstract*—Maximizing the coherent processing interval (CPI) is crucial when performing passive radar detection on weak signal reflections. In practice however, the CPI is limited by the target movement. In this work, the extent of the range and Doppler migration effects occurring when using a long CPI to integrate the returns from an L-band digital aeronautical communication system (LDACS) based passive radar is studied. In particular, our simulations underline the extensive Doppler migration effect that arises even for non-accelerating targets. To this end, the Keystone transform and fractional Fourier transform techniques are combined with the standard passive radar processing to enable the compensation of both range and Doppler migration effects. This non-model based approach is, however, shown to have limitations, in particular for low signal-to-noise ratios and/or multi-target scenarios. To address these shortcomings, a novel model-based framework that allows to perform joint target detection and parameter estimation is developed. For this, a super-resolution sparse Bayesian learning approach is employed. This technique uses a multi-target observation model which accurately accounts for the underlying range and Doppler migration effects and provides super-resolution estimation capabilities. This is particularly advantageous in the LDACS case since the narrow bandwidth generally limits the separation of closely spaced targets. The simulation experiments demonstrate the effectiveness of the algorithm and the advantages it provides when compared to the standard migration compensation approach.**

***Index Terms*—coherent processing, range and Doppler migration, LDACS, passive radar, keystone transform, fractional Fourier transform, FrFT, sparse Bayesian learning, super-resolution**

I. Introduction

The signal-to-noise ratio (SNR) at the matched filter output, while central to the radar operation in general, is particularly crucial for passive radar systems where weak signal reflections are used for target detection and estimation purposes. Since the output SNR is directly proportional to the coherent processing interval (CPI) employed, maximizing the CPI is essential for reliable passive radar operation. The CPI duration is nevertheless limited by the target motion and by the dimensions of the radar resolution cell. Using a long CPI can result in the target migrating over multiple cells, resulting in an energy dispersion and leading to "migrated" parameter estimates.

Traditionally, to benefit from a long CPI, the migration effects associated with the target movement need to be compensated. Various works in the literature have addressed the topic of migration compensation in radar systems. While the majority of these works have been primarily developed for synthetic aperture radar (SAR) and pulsed radar systems [1]–[7], some efforts have been made to apply these techniques also to passive radar systems [8]–[14].

The problem of linear range migration (RM) has been addressed, among others, in [1], [2], [8], [11], [14]. The Keystone transform (KT) is one of the most commonly used techniques since it allows for correcting the linear RM caused by a constant target velocity. This is achieved without a-priori velocity information by appropriately rescaling the time dimension. Additionally, some research works have also considered the correction of the quadratic RM and Doppler frequency migration (DFM) effects induced by a constant target acceleration [3]–[7], [9], [10], [12], [15]. Most of these works are directed at the detection or imaging of high-speed maneuvering targets in pulsed radar or SAR systems. Nevertheless, the impact of these effects is particularly crucial, even for non-accelerating targets, also in passive radar systems with a long CPI [10]. This is due to the high Doppler resolution and the bistatic Doppler shift variations which result in a relative geometry-induced acceleration and lead to DFM and quadratic RM effects. The compensation challenge arises here from the coupling of the RM and DFM effects. For the single target case, the migration effects can be decoupled if they are compensated for in a specific order [5]. This allows for the quadratic and linear RM to be corrected using two KT operations with the same time rescaling [5]. In between the KT operations, the DFM chirp component is compensated after using, e.g., fractional Fourier transform (FrFT), to estimate the chirp rate. The compensation of both RM and DFM for single target passive radar scenarios has been addressed in [9], [10], [12], [13], [15], [16].

Comparatively, in a multi-target case the superposition of chirps and the coupling of the RM and DFM effects make the overall compensation routine very challenging. In the radar literature, the multi-target scenario has been often considered in conjunction with the simplified assumptions that: a) only linear RM is present [1], [2], b) only DFM is present [17], [18], c) RM-DFM coupling is not accounted for [9], or d) successive target RM and DFM compensation, detection, and cancellation is enabled by model-based CLEAN-like schemes [3], [6], [7], [19], [20]. The CLEAN-type algorithms aim to successively detect and remove the contributions of the strong targets from the received signal such that to allow for detecting any weaker targets. Nevertheless, we note that, especially in passive radar scenarios, the low input SNR and/or resolution limitations impose considerable challenges towards: i) obtaining reliable chirp rate estimates using FrFT-like techniques for DFM compensation, and ii) successfully applying CLEAN since its performance is largely impacted by inaccurate estimates.

A passive radar based on the L-band digital aeronautical communication system (LDACS) is intended to provide accurate backup non-cooperative surveillance for critical civil aviation scenarios. These encompass, e.g., a transponder malfunction or shut down, or the need for non-cooperative aircraft localization [21]. Unlike other signals of opportunity, the LDACS signals are dedicated aeronautical communication signals, transmitted in aviation safety allocated frequency bands, and already directed towards the sky. The low transmit power of the LDACS system limits however the achievable detection performance. In this work, we first assess the extent of the migration effects when using a long CPI in an LDACS-based bistatic passive radar. Assuming non-accelerating targets, the small geometry-induced relative acceleration is shown to give rise to extensive DFM effects. To allow for a coherent SNR increase, we combine the KT and FrFT with the standard passive radar processing such that to compensate for the linear RM, quadratic RM, and DFM effects. Although a successful migration compensation is enabled for single target scenarios and ideal SNR conditions, the FrFT accuracy of the chirp rate estimate is not sufficient to fully compensate for the DFM in low input SNR conditions. Moreover, multi-target scenarios also pose challenges to this compensation approach.

We are therefore interested to address the shortcomings of this non-model based migration compensation approach using a model-based approach. In [22] we used a super-resolution (SR) sparse Bayesian learning (SBL) scheme to perform joint target detection and parameter estimation while accounting only for the linear RM. In this paper, we extend our work in [22] such that to employ a multi-target observation model accurately characterizing the linear RM, quadratic RM, and DFM effects. The resulting SR-SBL model-based approach is intrinsically a generalization of CLEAN, implementing successive interference cancellation, however, using non-discretized parameter estimates while also imposing sparsity constraints and successively updating the targets' parameters.

A sparse Bayesian estimation approach for migrating targets has been previously considered in [23] in the context of using a wideband pulsed-Doppler radar with a low pulse repetition frequency. The work in [23] was aimed at using the linear RM information to unambiguously measure the target velocity. By contrast, we consider the problem of jointly detecting and estimating targets in a narrowband passive radar scenario, that is, a scenario in which the signal bandwidth is much smaller than the carrier frequency. While the use of a long CPI leads to the same linear RM effects as in [23], in our case no velocity ambiguities arise due to the appropriately chosen segment length. However, DFM plays an important role and needs to be accounted for. Moreover, in our case the parameter space is not discretized and the variational Bayesian (VB) framework is used to construct an analytical approximation to the posterior distribution while in [23] a numerical approximation is employed.

A sparsity-driven approach was also considered in [17] in the context of estimating the parameters of multiple closely spaced and migrating targets. Nevertheless, the work in [17] assumes a passive multistatic SAR geometry and only accounts for the target DFM. Also, the parameter space is discretized and the multiple bistatic links are used to formulate the parameter estimation as a group sparse reconstruction problem.

The main contributions of our work are given as follows:

1) We study the extent of the RM and DFM effects, arising when using a long CPI to integrate the returns from a medium velocity target, e.g., commercial aircraft with average cruising speed between 205-255 m/s, using LDACS radar simulated data and develop an analytical framework to analyze the origin of the migration effects.
2) We combine state-of-the-art KT and FrFT techniques to jointly compensate for the linear RM, quadratic RM, and DFM effects for single target scenarios. The effectiveness of this non-model based method with regards to the coherent target SNR increase as well as its limitations in low SNR and/or multiple target scenarios are assessed.
3) We develop an observation model which accurately characterizes the signals in terms of both RM and DFM effects and establish a novel model-based framework for performing joint multi-target detection and parameter estimation. Since the parameter space is not discretized, this also allows for SR estimation capabilities.

The remainder of the paper is organized as follows. The signal and system model are introduced in Section II. The cross-ambiguity function (CAF) evaluation, the fast-time/slow-time representation, and the analytical framework used to analyze the migration effects are the subject of Section III. The KT and FrFT are combined to allow for a complete RM and DFM compensation in single target scenarios in Section IV. The SR-SBL approach, performing joint detection and parameter estimation while accounting for the RM and DFM, is developed for multi-target scenarios in Section V. Section VI concludes this work.

II. Signal and System Model

A. Transmit Signal Model

In this work, we consider a classical OFDM transmit signal model. The baseband representation of the signal emitted by the LDACS ground station is given as [24]:

$$s(t) = \sum_{l=0}^{L-1} \sum_{k=-N_u/2}^{N_u/2} c_{k,l} e^{j2\pi k \Delta f (t - T_{cp} - lT_s)} w(t - lT_s) \ , \quad 0 \leq t < LT_s + T_w \ , \tag{1}$$

where L is the number of OFDM symbols, N_u is the number of subcarriers, $c_{k,l}$ are the transmitted symbols, $\Delta f = 1/T_u$ is the subcarrier spacing, and T_u is the useful OFDM symbol duration. The variable $T_s = T_u + T_w + T_g$ denotes the total symbol duration, T_g is the guard-interval length, and $w(t)$ is a standard raised-cosine window with roll-off factor α_{roll} and duration $T_w = \alpha_{\text{roll}} T_s$. The LDACS transmission parameters are summarized in Table I [24].

B. Bistatic Radar Geometry

To characterize the bistatic radar geometry we make use of the North-referenced coordinate system in Fig. 1. The ranges R_T and R_R are the transmitter (TX)-to-target and target-to-receiver (RX) ranges. Parameter L_b is the baseline distance

This article has been accepted for publication in a future issue of this journal, but has not been fully edited. Content may change prior to final publication. Citation information: DOI 10.1109/TAES.2020.3026844, IEEE Transactions on Aerospace and Electronic Systems

TABLE I: LDACS Signal Transmission Parameters

Parameter	Value
Bandwidth (B)	500 kHz
Carrier frequency (f_c)	971.5 MHz
Subcarriers used (N_u)	50
Total symbol duration (T_s)	120 µs
Useful symbol duration (T_u)	102.4 µs
Guard interval duration (T_g)	4.8 µs
Window roll-off factor (α_{roll})	0.107

between the TX and RX, while θ_R and θ_T are the RX and TX look angles. The bistatic angle is β and ϕ measures the angle between the velocity vector and the bistatic bisector.

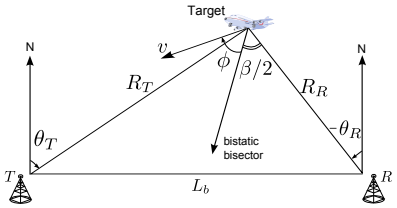

Fig. 1: Bistatic radar geometry in the North-referenced coordinate system

C. Reflected Signal Model

The passband LDACS transmit signal $\hat{s}(t)$ is modeled as

$$\hat{s}(t) = s(t)e^{j2\pi f_c t} \ . \tag{2}$$

Assuming that the direct path interference has already been removed at the RX, the received passband signal $\hat{r}(t)$, after being reflected from one moving point target, is a noisy, attenuated, and time delayed version of $\hat{s}(t)$ [25]:

$$\begin{aligned}\hat{r}(t) &= \alpha\hat{s}(t-\tau(t)) + \hat{\psi}(t) \\ &= \alpha s(t-\tau(t))e^{j2\pi f_c(t-\tau(t))} + \hat{\psi}(t) \ .\end{aligned} \tag{3}$$

In (3), α denotes the complex attenuation coefficient, $\hat{\psi}(t)$ is the passband complex additive white Gaussian noise, and $\tau(t)$ is the varying bistatic delay. The extent of variation in $\tau(t)$ depends on the target movement during the CPI duration T. This becomes significant for long T and/or fast moving targets. Assuming that the target range $R(t)$ is such that $dR(t)/dt \ll c$, where c is the speed of light, $\tau(t)$ can be expressed as [26]

$$\tau(t) = \tau_0 - \frac{\nu_0}{f_c}t + \frac{a_0}{2c}t^2 \ , \tag{4}$$

where τ_0 is the initial bistatic delay, a_0 is the geometry-induced acceleration, and ν_0 is the initial bistatic Doppler shift

$$\frac{\nu_0}{f_c} = \frac{2v}{c}\cos(\phi_0)\cos\left(\frac{\beta_0}{2}\right) \ , \tag{5}$$

where β_0 and ϕ_0 denote the initial angles (see Fig. 1). Inserting (4) in (3), received signal $\hat{r}(t)$ is expressed as [25]

$$\begin{aligned}\hat{r}(t) = \alpha s\left(t - \left(\tau_0 - \frac{\nu_0}{f_c}t + \frac{a_0}{2c}t^2\right)\right) \times \\ e^{j2\pi f_c\left(t-\left(\tau_0-\frac{\nu_0}{f_c}t+\frac{a_0}{2c}t^2\right)\right)} + \hat{\psi}(t) \ ,\end{aligned} \tag{6}$$

which after demodulation results in the baseband model:

$$\begin{aligned}r(t) = \alpha e^{-j2\pi f_c\tau_0}s\left(t-\tau_0+\frac{\nu_0}{f_c}t-\frac{a_0}{2c}t^2\right)\times \\ e^{j2\pi\nu_0 t}e^{-j2\pi f_c\frac{a_0}{2c}t^2} + \psi(t) \ .\end{aligned} \tag{7}$$

From (7), we see that the Doppler effect is reflected in: i) the time scaling of the complex envelope and ii) the carrier frequency shift. Intuitively, the time compression/dilation arises due to the target moving towards/further away from the TX/RX during the CPI. This results in a varying bistatic range and can give rise to RM effects [25]. The condition under which the target velocity induced RM effects can be neglected is a function of the time-bandwidth (TB) product [25], [26]:

$$T\frac{\nu_0}{f_c} \ll \frac{1}{B} \rightarrow TB \ll \frac{f_c}{\nu_0} \text{ , practically } TB \leq \frac{f_c}{10\nu_0} \ . \tag{8}$$

Similarly, the condition under which the impact of the target acceleration on the complex envelope can be neglected is [26]:

$$T^2\frac{a_0}{2c} \ll \frac{1}{B} \rightarrow T^2B \ll \frac{2c}{a_0} \text{ , practically } T^2B \leq \frac{2c}{10a_0} \ . \tag{9}$$

The equations (8) and (9) essentially state that the linear/quadratic RM effects are negligible when the change in the signal duration due to the target velocity/acceleration are smaller than the delay resolution. Similarly, the frequency shift induced by the complex exponential $e^{-j2\pi f_c\frac{a_0}{2c}t^2}$ is responsible for the DFM and can only be neglected as long as the associated velocity change is less than the velocity resolution

$$a_0T \ll \frac{\lambda}{2T} \rightarrow T \ll \sqrt{\frac{\lambda}{2a_0}} \ . \tag{10}$$

With a passive radar, target detection and parameter estimation are traditionally performed by evaluating the CAF, i.e., correlating $r(t)$ with delayed and Doppler shifted versions of the reference[1] transmit signal $s(t)$. In what follows, we formally introduce the CAF and its connection to the migration effects.

III. CAF and Migration Effects

A. CAF Evaluation

The CAF is expressed as

$$\chi_{\text{CAF}}(\tau_H,\nu_H) = \int_0^T r(t)s^*(t-\tau_H)e^{-j2\pi\nu_H t}dt \ , \tag{11}$$

where $0 \leq \tau_H \leq \tau_{\text{max}}$, $-\nu_{\text{max}} \leq \nu_H \leq \nu_{\text{max}}$, while τ_{max} and ν_{max} denote the maximum expected delay and Doppler shift. In this work, we use the fast-time/slow-time representation well known from the pulsed radar to evaluate (11). This representation allows to compute an efficient approximation to the CAF in (11) while also providing a framework to analyze the migration effects [27].

Signal $s(t)$ is assumed to consist of N_{seg} contiguous segments, each of duration T_r and consisting of L_{seg} samples. For sampling frequency f_s, $T_r = L_{\text{seg}}/f_s$ and $T = L_{\text{seg}}N_{\text{seg}}/f_s$.

[1]We assume that a separate (possibly cable) transmission is available to make the LDACS reference signal accessible at the RX. Employing a directional antenna to collect the direct signal would not help in this case since both reference and surveillance antennas would be directed at the sky.

This article has been accepted for publication in a future issue of this journal, but has not been fully edited. Content may change prior to final publication. Citation information: DOI 10.1109/TAES.2020.3026844, IEEE Transactions on Aerospace and Electronic Systems

The segments are zero-padded with $L_{\max} = \tau_{\max} f_s$ samples and arranged as the columns of a matrix $\mathbf{S}$. Furthermore, $r(t)$ is divided in N_{seg} segments of duration $T_r + \tau_{\max}$, with each two adjacent segments having an overlap of $L_{\max}$ samples, arranged as the columns of another matrix $\mathbf{R}$, see also Fig. 2. The overlap is needed to ensure that the m^{th} transmit segment is "found" in the m^{th} receive segment.

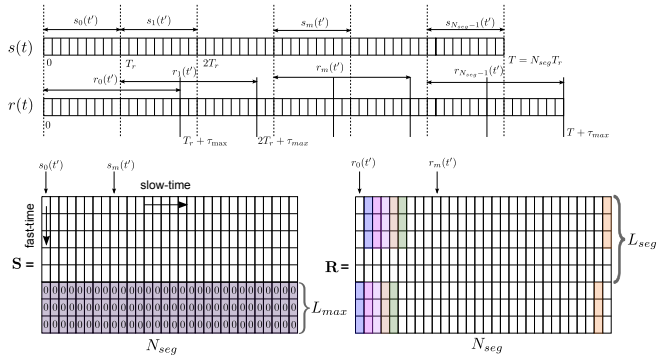

Fig. 2: Batches signal segmentation procedure used to evaluate the CAF (adapted from [27])

Assuming that for small values of $T_r \times \nu_{\max}$ the Doppler shift within a segment is constant, the Batches approximation to (11) can be expressed as [27]

$$\chi^{b}_{\text{CAF}}(\tau_H, \nu_H) = e^{-j2\pi\nu_H T_r/2} \sum_{m=0}^{N_{\text{seg}}-1} e^{-j2\pi\nu_H m T_r} \times \int_0^{T_r+\tau_{\max}} r_m(t') s^*_m(t'-\tau_H) dt' \ , \tag{12}$$

where t' denotes the *fast-time*, m is the discrete *slow-time*, related as $t = t' + mT_r$, and $r_m(t')$ and $s_m(t')$ are the m^{th} receive and transmit segments [27]. Compared to (11), the Doppler mismatch introduced within each block in (12) leads to an SNR loss which is a function of the target Doppler shift and of the ambiguity function of the transmit segments [27]. The number of samples L_{seg} is generally chosen such that: a) the Doppler shift is unambiguous, $\nu_{\max} < 1/(2T_r) = f_s/(2L_{\text{seg}})$ and b) the SNR loss at $\nu_{\max}$ is less than 1 dB. A general "rule of thumb" to ensure the latter has been given in [11] for phase-shift keying signals as: $L_{\text{seg}} < f_s/(3.824\ \nu_{\max})$. To obtain the delay-Doppler response from (12) we compute:

1) The cross-correlations between $r_m(t')$ and $s_m(t')$
2) The FT along slow-time index m.

Next, we assess the extent of the migration effects when coherently integrating the LDACS returns over a long CPI. To simulate the LDACS received signal we use the Flexible, Extensible Radar and Sonar Simulator (FERS) from [28], [29]. The input LDACS signal is a simplified LDACS version with pilot symbols replaced by independent and identically distributed (IDD) symbols. Also, an oversampled version with $f_s = 1.25$ MHz is used to generate accurate results in FERS. The mean power of the oversampled samples is normalized to match the energy of the LDACS signal sampled at the bandwidth B. As radar simulator parameters, we use $P_T^{\text{ov}} = \frac{P_T G_T G_R}{L_T L_R} = 158\ W$ to denote the combined transmit power together with unit efficiency isotropic antennas and no system losses. The equivalent noise temperature is $T_e = 578\ K$ and corresponds to a 3 dB RX noise figure. The bistatic parameters are summarized in Table II. The delay-Doppler plots obtained when evaluating (12) using the processing parameters in Table III are presented in Fig. 3a for a stationary target and in Fig. 3b for a moving target.

TABLE II: Bistatic geometry parameters

Parameter	Value
$R_{R,0}$	25.25 km
$R_{T,0}$	30.2 km
L_b	26.4 km
τ_0	184.97 μs
β_0	56.0189°
ϕ_0	34.9671°
ν_0	990.79 Hz
v	211.2975 m/s

TABLE III: Processing and input parameters

Parameter	Value
T	4 s
f_s	1.25 MHz
N_s	5×10^6
L_{seg}	200
N_{seg}	25000
$L_{\max}$	400
$\lvert\alpha\rvert^2$	-178.84 dB
σ_s^2	-5.27 dB
$\sigma_\psi^2 = N_R$	-143 dB
SNR_{in}	-41.1 dB

The stationary response is concentrated at the true target delay and 0 Hz Doppler shift. Comparatively, in the moving case the energy is dispersed over multiple cells and both RM and DFM are clearly observed. To better interpret the results in Fig. 3, we first assess the input SNR, denoted as SNR_{in}, as the average signal SNR at the RX input

$$\text{SNR}_{\text{in}} = \frac{\lvert\alpha\rvert^2 \sigma_s^2}{\sigma_\psi^2} \ , \tag{13}$$

where $\lvert\alpha\rvert^2$ is the attenuation parameter, σ_s^2 is the average power of an LDACS signal sample, and $\sigma_\psi^2 = N_R = k_B T_e B_{\text{eff}}$ is the thermal noise power at the RX. All input parameters are summarized in Table III, where we note that the noise bandwidth considered is specific to FERS, i.e., $B_{\text{eff}} = f_s/2$. Next, we introduce SNR_{out} as the peak output SNR after correlation processing, as given by $\lvert\chi_{\text{CAF}}(\tau_H, \nu_H)\rvert^2$ from (11). Intuitively, the peak instantaneous output power occurs when the filter is perfectly matched, i.e., $(\tau_H, \nu_H) = (\tau_a, \nu_a)$. Also, the average output noise power, i.e., the noise floor, is given by the correlation between the white noise and the signal samples. For N_s processed samples, SNR_{out} takes the form

$$\text{SNR}_{\text{out}} = \frac{\left| \alpha \sum_{n=1}^{N_s} \lvert s(n)\rvert^2 \right|^2}{\mathbb{E}\left\{ \left| \sum_{n=1}^{N_s} \psi(n) s^*(n) \right|^2 \right\}} = \frac{\lvert \alpha N_s \sigma_s^2 \rvert^2}{N_s \sigma_\psi^2 \sigma_s^2} = \frac{\lvert\alpha\rvert^2 \sigma_s^2}{\sigma_\psi^2} N_s \ , \tag{14}$$

clearly depicting the expected coherent integration gain N_s

$$\text{SNR}_{\text{out}} = \text{SNR}_{\text{in}} \times N_s \ . \tag{15}$$

The ideally expected output SNR parameters, given by (14), are summarized in Table IV along with the actually measured ones for both the stationary and moving target scenarios. In the stationary case the Batches algorithm is an exact implementation of the CAF and the measured quantities closely

This article has been accepted for publication in a future issue of this journal, but has not been fully edited. Content may change prior to final publication. Citation information: DOI 10.1109/TAES.2020.3026844, IEEE Transactions on Aerospace and Electronic Systems

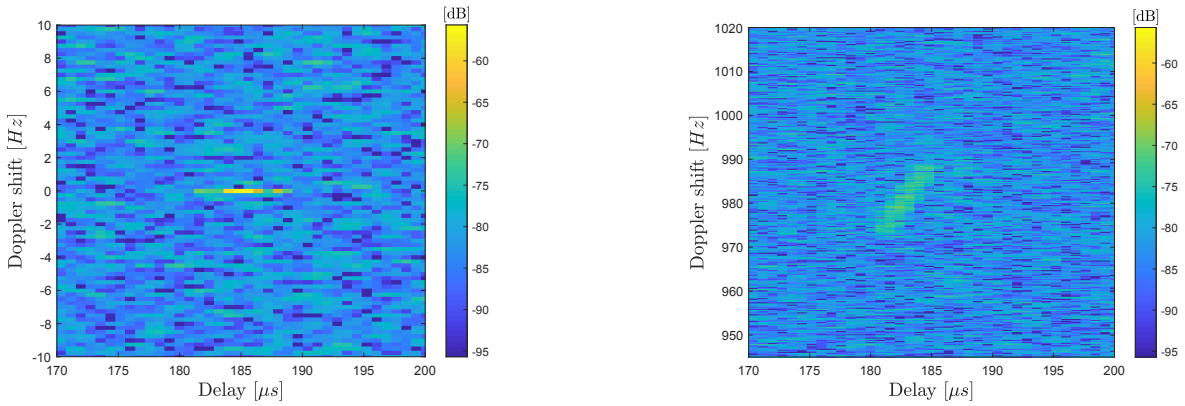

(a) Stationary target (b) Moving target

Fig. 3: $|\chi_{\text{CAF}}(\tau_H, \nu_H)|^2$ - Delay-Doppler response, T = 4 s

TABLE IV: Ideal vs. measured output SNR parameters

Parameter	Peak signal power	Noise floor	SNR_{out}	Integration gain
Ideal	-55.4 dB	-81.3 dB	25.88 dB	66.98 dB
Measured - stationary target	-55.69 dB	-81.3 dB	25.59 dB	66.69 dB
Measured - moving target	-69.3 dB	-81.3 dB	12 dB	53.1 dB

match the predicted ones. The slight peak power loss is due to the delay discretization and its extent is reduced here due to oversampling. The expected noise floor is consistent with averaging the CAF responses in both Fig. 3a and Fig. 3b. Comparatively, in the moving scenario the target energy is dispersed over multiple range and Doppler cells and the delay and Doppler shift estimates are "migrated" from the true ones. Accounting for both RM and DFM effects is therefore crucial to allowing for a coherent SNR increase.

B. Range and Doppler Migration

The migration effects are classified as a function of the target motion characteristics as [7]: i) linear RM for constant velocity, and ii) quadratic RM and second order DFM for constant acceleration. To inspect their origin, we start with the integral in (12), denoting the cross-correlation over segment m in the fast-time slow-time (ftst) domain, rewritten as

$$\mathbf{X}_{\text{ftst}}(t', m) = \int_{0}^{T_r+\tau_{\max}} r_m(y) s_m^*(y - t') dy \,. \tag{16}$$

Due to the segmentation used to obtain $r_m(y)$ from $r(t)$, evaluating (16) is not straightforward. Following the derivations in Appendix A, (16) can be expressed in the fast-frequency slow-time (ffst) domain as in (17), with $X_m(f-\nu_0)$ denoting the cross-terms contribution due to the Batches processing. The last three exponential terms in (17) depict the origin of the linear RM, quadratic RM, and DFM. The RM arises due to the coupling between fast-frequency f and slow-time m or m^2. This implies that the signal phase changes differently with respect to slow-time for each fast-frequency [11]. The DFM chirp in (17) arises due to the large bistatic Doppler shift variations and high Doppler resolution. In what follows, we address the compensation of these migration effects.

IV. Range and Doppler Migration Compensation

Conventional approaches aim to correct for the RM and DFM. The starting point for this is (17), given in discrete form as

$$\mathbf{X}_{\text{ffst}}[k, m] = \alpha_{k,m} e^{-j2\pi f_k \tau_0} \times e^{j2\pi\nu_0\left(\frac{f_k+f_c}{f_c}\right)mT_r} e^{-j2\pi\frac{a_0}{2\lambda}\left(\frac{f_k+f_c}{f_c}\right)(mT_r)^2} \,, \tag{18}$$

where $k = 0, \cdots, K-1$ is the fast-frequency bin, $K = N_{\text{FFT,ft}}$, $\alpha_{k,m} = \alpha e^{-j2\pi f_c \tau_0} \left[(S_m(f_k - \nu_0) + X_m(f_k - \nu_0)) S_m^*(f_k)\right]$, and the k^{th} fast-frequency sub-band, f_k, is given as:

$$f_k = \begin{cases} \frac{k}{K} f_s, & 0 \le k \le K/2 - 1 \\ \frac{k-K}{K} f_s, & K/2 \le k \le K - 1 \end{cases} . \tag{19}$$

The linear RM, quadratic RM, and DFM effects, all coupled through m, can be compensated for in 3 steps as follows [5]:

1) Apply the Keystone transform to (18) to compensate for the quadratic RM by rescaling the slow-time $m \longrightarrow m\sqrt{\frac{f_c}{f_k+f_c}}$. The compensated response is $\mathbf{X}^1_{\text{ffst}}[k, m]$:

$$\begin{aligned}\mathbf{X}^1_{\text{ffst}}[k, m] &= \widehat{\alpha}_{k,m} e^{-j2\pi f_k \tau_0} e^{j2\pi\nu_0\left(\frac{f_k+f_c}{f_c}\right)m\sqrt{\frac{f_c}{f_k+f_c}}T_r} \times \\ &\quad e^{-j2\pi\frac{a_0}{2\lambda}\left(\frac{f_k+f_c}{f_c}\right)m^2\left(\frac{f_c}{f_k+f_c}\right)T_r^2} \\ &= \widehat{\alpha}_{k,m} e^{-j2\pi f_k \tau_0} \underbrace{e^{j2\pi\nu_0\sqrt{\frac{f_k+f_c}{f_c}}mT_r}}_{\text{leftover linear RM}} \underbrace{e^{-j2\pi\frac{a_0}{2\lambda}m^2T_r^2}}_{\text{DFM}}\end{aligned} \tag{20}$$

$$\mathbf{X}_{\text{ffst}}(f, m) = \alpha \left[(S_m(f-\nu_0) + X_m(f-\nu_0)) S_m^*(f)\right] e^{-j2\pi f_c \tau_0} e^{-j2\pi f \tau_0} \underbrace{e^{j2\pi\nu_0\left(\frac{f+f_c}{f_c}\right)mT_r}}_{\text{linear RM}} \underbrace{e^{-j2\pi\frac{a_0}{2\lambda}\frac{f}{f_c}(mT_r)^2}}_{\text{quadratic RM}} \underbrace{e^{-j2\pi\frac{a_0}{2\lambda}(mT_r)^2}}_{\text{DFM}} + \Psi_m(f) S_m^*(f) \,. \tag{17}$$

2) Employ the fractional Fourier transform to estimate the chirp rate $-\frac{a_0}{\lambda}$ in (20) and use it to compensate for the DFM chirp. Accounting for the first two compensation steps, we obtain:

$$\begin{aligned}\mathbf{X}_{\text{ffst}}^{1,2}[k,m] &= \widehat{\alpha}_{k,m} e^{-j2\pi f_k \tau_0} e^{j2\pi\nu_0\sqrt{\frac{f_k+f_c}{f_c}}mT_r} \times \\ &\quad e^{-j2\pi\frac{a_0}{2\lambda}m^2T_r^2} e^{j2\pi\frac{\widehat{a}_0}{2\lambda}m^2T_r^2} \\ &= \widehat{\alpha}_{k,m} e^{-j2\pi f_k\tau_0} e^{j2\pi\nu_0\sqrt{\frac{f_k+f_c}{f_c}}mT_r}, \text{for } a_0=\widehat{a}_0 \quad (21)\end{aligned}$$

3) Finally, apply a second Keystone transform to (21) to compensate for the remaining linear RM by rescaling the slow-time again $m \longrightarrow m\sqrt{\frac{f_c}{f_k+f_c}}$. The overall response, incorporating all 3 compensation steps, is:

$$\begin{aligned}\mathbf{X}_{\text{ffst}}^{1,2,3}[k,m] &= \widehat{\alpha}_{k,m} e^{-j2\pi f_k\tau_0} e^{j2\pi\nu_0\sqrt{\frac{f_k+f_c}{f_c}}m\sqrt{\frac{f_c}{f_k+f_c}}T_r} \\ \mathbf{X}_{\text{ffst}}^{1,2,3}[k,m] &= \widehat{\alpha}_{k,m} e^{-j2\pi f_k\tau_0} e^{j2\pi\nu_0 mT_r} \ . \quad (22)\end{aligned}$$

The compensated response in (22) describes a non-migrated target at (τ_0, ν_0). We note that weight $\widehat{\alpha}_{k,m}$ in (22) can differ from $\alpha_{k,m}$ in (18) since it is also implicitly re-sampled by the KT [14]. Next, we shortly introduce how the two transforms are implemented for the purpose of this work.

A. Keystone Transform (KT)

Different methods can be used to implement the KT [2], [9], [11], [14], among which we note the sinc-based interpolation and the chirp-Z transform (CZT). The CZT in particular exhibits a very low complexity and is the method of choice in this work. Formally, the CZT of signal $x(n)$ computes the M length z-transform along spiral contours in the z-plane [30]

$$\text{CZT}\{x(n)\} = C(m) = \sum_{n=0}^{N_s-1} x(n) z_m^{-n} \ , \quad (23)$$

where $m = 0, \cdots, M-1$, $z_m = A \times W^{-m}$ defines the contour of interest, $A = A_0 e^{j2\pi\theta_0}$is the starting point of the contour, and $W = W_0 e^{j2\pi\phi_0}$ gives the sample spacing on the contour. To allow for an efficient implementation of the CZT using FFT operations, (23) is computed as in [30]. The input signals for the CZT-based KT operation in Step 1) are the rows of $\mathbf{X}_{\text{ffst}}$ in (18). Since the CZT delivers the re-sampled signal in the slow-frequency domain, an additional IFFT operation is required after the CZT to return to slow-time before the DFM compensation in Step 2). The input signals to the CZT-based KT operation in Step 3) are the rows of $\mathbf{X}_{\text{ffst}}^{1,2}$ in (21). The CZT parameters are summarized in Table V.

TABLE V: CZT parameters

Parameter	Value
$N_s = M$	N_{seg}
$A_0 = W_0$	1
θ_0	1
$\phi_{0,k}$	$-\sqrt{\frac{f_k+f_c}{f_c}}\frac{1}{M}$
Inputs	$\begin{cases}\mathbf{X}_{\text{ffst}}[k,:] \\ \mathbf{X}_{\text{ffst}}^{1,2}[k,:]\end{cases}$

TABLE VI: FRFT parameters

Parameter	Value
λ	0.3086 m
N_s	$N_{\text{seg}} = M$
PRF	$1/T_r$
α_{rot}	$a_{\text{rot}} \times \frac{\pi}{2}$
a_{rot}	$\in [0.99, 1)$
Δa_{rot}	10^{-4}
Inputs	$\mathbf{X}_{\text{ffst}}^{1}[k,:]$

B. Fractional Fourier Transform (FrFT)

The FrFT is a generalization of the classical FT characterized by the rotation angle α_{rot}. It provides numerous advantages when analyzing chirp signals [18], [31]–[33], since, for an optimum α_{rot}, projecting a chirp onto the FrFT concentrates its energy in a single impulse and maximizes its amplitude. Also, the FrFT is a linear transform, which implies that no cross-terms are introduced for multi-target scenarios.
The FrFT of a generic chirp signal $x(t) = e^{j\pi(\varphi_0+2f_0t+c_rt^2)}$ with chirp rate $c_r = a_o/\lambda$ is defined as a function of the kernel function $K(\alpha_{\text{rot}}, u, t)$ such that [32]

$$X_{\alpha_{\text{rot}}}(u) = \mathcal{F}_{\alpha_{\text{rot}}}\{x(t)\} = \int_{-\infty}^{\infty} K(\alpha_{\text{rot}}, u, t) x(t) dt \ , \text{ where} \quad (24)$$

$$K(\alpha_{\text{rot}}, u, t) = \quad (25)$$
$$\begin{cases}\sqrt{\frac{1-j\cot\alpha_{\text{rot}}}{2\pi}}\exp^{j\frac{\cot\alpha_{\text{rot}}}{2}(u^2+t^2)}\exp^{-j\frac{u}{\sin\alpha_{\text{rot}}}t}, & \alpha_{\text{rot}} \neq n\pi \\ \delta(t-u), & \alpha_{\text{rot}} = n2\pi \\ \delta(t+u), & \alpha_{\text{rot}} + \pi = n2\pi\end{cases} .$$

Generally, α_{rot} is given as a function of the signal chirp rate, number of samples N_s, and sampling frequency PRF [33]

$$\alpha_{\text{rot}} = \frac{\pi}{2} + \tan^{-1}\left(\frac{N_s}{\text{PRF}^2}\frac{a_0}{\lambda}\right) \ . \quad (26)$$

To obtain the chirp rate of interest, we first estimate the optimum $\alpha_{\text{rot}}^{\text{opt}}$ by analyzing the FrFT magnitude which is maximized when the chirp spectrum is most compact [34]. While the FrFT can be performed on any row of $\mathbf{X}_{\text{ffst}}^1$, to allow for an increased accuracy for low input SNR conditions, the FrFT-based estimation is applied to all the rows such that

$$\alpha_{\text{rot}}^{\text{opt}} = \arg\max_{\alpha_{\text{rot}}} \max_k \max_u \left|\mathbf{X}_{\alpha_{\text{rot}}}^k(u)\right| . \quad (27)$$

To evaluate the FrFT we use the algorithm in [35]–[37] and map the search range for α_{rot} in (27) to realistic accelerations. Defining $\alpha_{\text{rot}} = a_{\text{rot}} \times \frac{\pi}{2}$ we rewrite (26) as a function of $\widehat{a}_0$:

$$\widehat{a}_0 = -\left[\tan\left((a_{\text{rot}}-1)\frac{\pi}{2}\right)\frac{\lambda}{MT_r^2}\right] \ . \quad (28)$$

Generally $a_{\text{rot}} \in [0, 4)$ [34]. Evaluating (28) for the specific parameters in Table VI, and accounting for the small relative accelerations of interest in this work, further reduces the search range to $a_{\text{rot}} \in [0.99, 1)$. The latter corresponds to $\widehat{a}_0 \in [0, 7.57)\ m/s^2$. Finding the optimum a_{rot} is achieved here by performing a linear search with a very fine increment Δa_{rot}. Alternatively, a coarse-to-fine approach [34] can be pursued.

C. Migration Compensation Routine

Let us now describe the overall compensation routine which is summarized in Algorithm 1. We start from (12) and incorporate the KT and FrFT such as to obtain the compensated response in (22). To assess the RM and DFM compensation capabilities, we consider both single and multi-target scenarios and apply Alg. 1 to the LDACS FERS radar simulated signal.

This article has been accepted for publication in a future issue of this journal, but has not been fully edited. Content may change prior to final publication. Citation information: DOI 10.1109/TAES.2020.3026844, IEEE Transactions on Aerospace and Electronic Systems

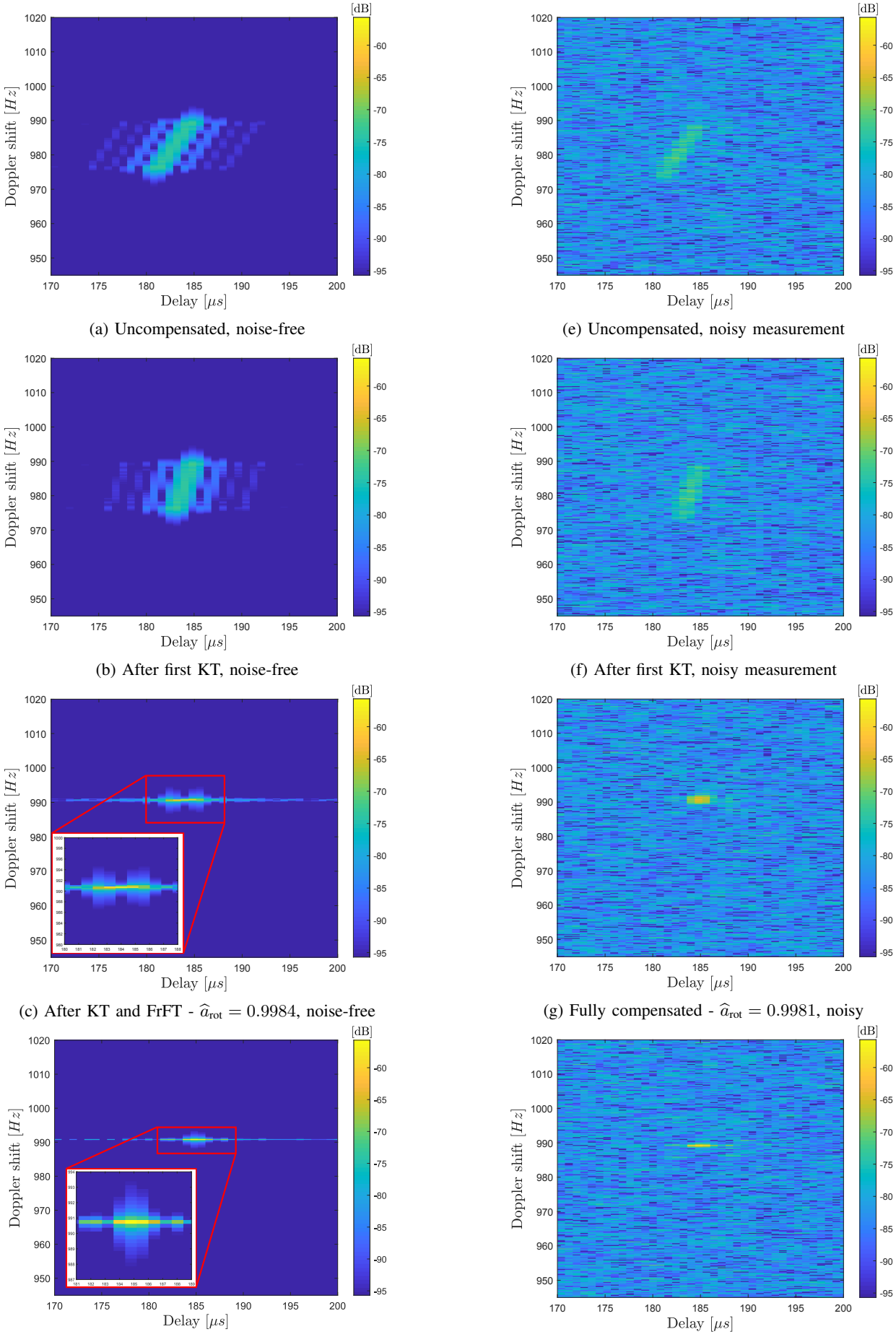

(a) Uncompensated, noise-free

(e) Uncompensated, noisy measurement

(b) After first KT, noise-free

(f) After first KT, noisy measurement

(c) After KT and FrFT - $\widehat{a}_{\text{rot}} = 0.9984$, noise-free

(g) Fully compensated - $\widehat{a}_{\text{rot}} = 0.9981$, noisy

(d) Fully compensated, noise-free

(h) Fully compensated - $\widehat{a}_{\text{rot}} = 0.9984$, noisy

Fig. 4: $|\chi_{\text{GAF}}(\tau_H, \nu_H)|^2$ - Delay-Doppler response at different stages, T = 4 s

1) Single Target: We start with a single target scenario and the ideal noise-free case. Figures 4a-4d depict the migration effects at different compensation stages. In the uncompensated response in Fig. 4a, extensive RM and DFM can be recognized. After the first KT, Fig. 4b shows a reduced RM when compared to Fig. 4a. Next, applying the FrFT results in Fig. 4c, where the DFM is compensated and only a residual RM is left. This step allows to obtain $\widehat{a}_0 = 1.2118\ m/s^2$, which becomes the "true" geometry induced acceleration. Finally, Fig. 4d shows the fully compensated response. The target energy is refocused at $(\widehat{\tau}_0,\ \widehat{\nu}_0)$ = $(184.8\ \mu s,\ 990.75$ Hz) with a peak response of -56 dB. When accounting for the small delay discretization and Batches approximation losses, this value closely matches the ideal prediction in Table IV.

Algorithm 1 Range and Doppler Migration Compensation

Select T, f_s, $\tau_{\max}$, and $\nu_{\max}$
Select L_{seg} to minimize SNR loss, avoid velocity ambiguity, and ensure no range migration within T_r
$N_{\text{seg}} \leftarrow \left\lceil \frac{T f_s}{L_{\text{seg}}} \right\rceil$ and $L_{\max} \leftarrow \tau_{\max} f_s$
Carry out segmentation and reshaping to obtain $\mathbf{S}$ and $\mathbf{R}$
$N_{\text{FFT,ft}} \leftarrow 2^{\text{nextpow2}(2\times L_{\text{seg}}+L_{\max}-1)}$ and $N_{\text{FFT,st}} \leftarrow N_{\text{seg}}$

Part 1 – Fast-frequency/slow-time

for $m = 1 : N_{\text{seg}}$ **do**
  $\mathbf{X}_{\text{ffst}}[:,m] \leftarrow \text{FFT}^*\{\mathbf{S}[:,m], N_{\text{FFT,ft}}\} \odot \text{FFT}\{\mathbf{R}[:,m], N_{\text{FFT,ft}}\}$
end for

Part 2 – First CZT-KT RM Compensation

$A \leftarrow 1$, $N_{\text{FFT,c}} \leftarrow 2^{\text{nextpow2}(2M-1)}$
for $k = 1 : N_{\text{FFT,ft}}$ **do**
  $W_k \leftarrow e^{-j\frac{2\pi}{M}\sqrt{\frac{f_c+f_k}{f_c}}}$
  $\mathbf{C}[k,:] \leftarrow \text{CZT}\{\mathbf{X}_{\text{ffst}}[k,:]\}$
end for
$\mathbf{X}^1_{\text{ffst}} \leftarrow \text{IFFT}\{\mathbf{C}, N_{\text{FFT,st}}, 2\}$

Part 3 – FrFT-based DFM Compensation

$a_{\text{rot}} = 0.99 : 10^{-4} : 0.999$, $\alpha_{\text{rot}} \leftarrow a_{\text{rot}} \times \pi/2$
for $r = 1 : \text{length}(a_{\text{rot}})$ **do**
  for $k = 1 : N_{\text{FFT,ft}}$ **do**
    $\mathbf{X}_{\alpha_{\text{rot}}}[k,:] \leftarrow \mathcal{F}_{\alpha_{\text{rot}}}\{\mathbf{X}_{\text{ffst}}[k,:]\}$
  end for
  $X_{a_{\text{rot}}}[r] = \max_k\ \max_u\ \mathbf{X}_{\alpha_{\text{rot}}}$
end for
$\widehat{a}_{\text{rot}} \leftarrow \arg\max_{a_{\text{rot}}}\{X_{a_{\text{rot}}}\}$
Compute acceleration estimate $\widehat{a}_0$ from $\widehat{a}_{\text{rot}}$ using (28)
$\mathbf{X}^{1,2}_{\text{ffst}}[k,m] \leftarrow \mathbf{X}^1_{\text{ffst}}[k,m]\, e^{j2\pi\frac{\widehat{a}_0}{2\lambda}m^2T_r^2}$

Part 4 – Second CZT-KT RM Compensation

$A \leftarrow 1$, $N_{\text{FFT,c}} \leftarrow 2^{\text{nextpow2}(2M-1)}$
for $k = 1 : N_{\text{fft,ft}}$ **do**
  $W_k \leftarrow e^{-j\frac{2\pi}{M}\sqrt{\frac{f_c+f_k}{f_c}}}$
  $\mathbf{X}^{1,2,3}_{\text{ffsf}}[k,:] \leftarrow \text{CZT}\left\{\mathbf{X}^{1,2}_{\text{ffst}}[k,:]\right\}$
end for

Part 5 – Compensated Delay-Doppler CAF Response

$\mathbf{X}_{\text{ftsf}} \leftarrow \text{IFFT}\left\{\mathbf{X}^{1,2,3}_{\text{ffsf}}, N_{\text{FFT,ft}}, 1\right\}$
$\mathbf{X}_{\text{ftsf}} \leftarrow \mathbf{X}_{\text{ftsf}}[1 : L_{\max},:]$
$\tau_H \leftarrow [0 : (L_{\max}-1)]/f_s$
$\nu_H \leftarrow \left[-\frac{N_{\text{FFT,st}}}{2} : \frac{N_{\text{fft,st}}}{2}-1\right] \times \frac{f_s}{L_{\text{seg}}}\frac{1}{N_{\text{FFT,st}}}$
$|\chi_{\text{CAF}}(\tau_H,\nu_H)|^2 \leftarrow |\mathbf{X}_{\text{ftsf}}[:,:]|^2$

Next, Figs. 4e-4h show the results obtained in the presence of noise. In particular with respect to the DFM compensation, our simulations confirmed the challenge underlined in [17] of obtaining an accurate chirp rate estimate. The low input SNR and the small acceleration lead to the estimation being very sensitive to the search interval and increment step used for a_{rot}. Using a reduced search $a_{\text{rot}} \in [0.997, 0.999]$ resulted in $\widehat{a}_{\text{rot}} = 0.9981$ and $\widehat{a}_0 = 1.439\ m/s^2$. Since this does not match the "true" noise-free value however, the DFM is not fully compensated in Fig. 4g and part of the energy remains dispersed, with the peak response reduced to -63.74 dB. By comparison, Fig. 4h shows the response when the "true" $\widehat{a}_0 = 1.2118\ m/s^2$ is used instead. The energy is mostly refocused with a -57 dB peak response, pointing to conclude that even a small inaccuracy in $\widehat{a}_0$ can lead to a 7 dB SNR loss.

2) Multiple Targets: Next, we consider a two-target scenario with parameters given as in Table VII. For simplicity, we look at the noise-free case only. The uncompensated delay-Doppler response is shown in Fig. 5a and depicts two targets impacted by both RM and DFM. The fully compensated response when applying Alg. 1 is shown in Fig. 5b. We observe that while the RM appears corrected for both targets, the DFM is only partially compensated for the second target. To better understand the cause, we look at the multi-target data model, which, using (18), can be expressed as:

$$\mathbf{X}_{\text{ffst}}[k,m] = \sum_{g=1}^{N_g} \alpha^g_{k,m} e^{-j2\pi f_k \tau_{0,g}} e^{j2\pi\nu_{0,g}\left(\frac{f_k+f_c}{f_c}\right)mT_r} \times e^{-j2\pi\frac{a_{0,g}}{2\lambda}\left(\frac{f_k+f_c}{f_c}\right)m^2T_r^2} + \Psi_m(f_k)S^*_m(f_k)\ , \quad (29)$$

where, g is the target index, N_g the total number of targets, and $\alpha^g_{k,m}, \tau_{0,g}, \nu_{0,g}$, and $a_{0,g}$ are the attenuation, initial delay, initial Doppler shift, and induced acceleration of target g, respectively. The two KT operations naturally affect all targets simultaneously, while the DFM compensation only works correctly if the targets experience the same acceleration. This is because the FrFT-based estimation of parameter a_{rot} chooses the one that maximizes the FrFT regardless of the total number of chirps. In our case, the slow-time signal consists of two superimposed chirps with rates $\widehat{a}_{0,1} = 1.2118\ m/s^2$ ($\widehat{a}_{\text{rot},1} = 0.9984$) and $\widehat{a}_{0,2} = 1.439\ m/s^2$ ($\widehat{a}_{\text{rot},2} = 0.9981$) as seen from the complete FrFT response in Fig. 5c.

Applying the steps in Alg. 1 to (29) and assuming $\frac{f_c}{f_c+f_k} \approx 1 - \frac{f_k}{f_c}$, we obtain the noise-free compensated response:

$$\mathbf{X}^{\text{comp}}_{\text{ffst}}[k,m] = \alpha^1_{k,m} e^{-j2\pi f_k\tau_{0,1}} e^{j2\pi\nu_{0,1}mT_r} + \alpha^2_{k,m} e^{-j2\pi f_k\tau_{0,2}} \times e^{j2\pi\nu_{0,2}mT_r} e^{-j2\pi\left(\frac{a_{0,2}-a_{0,1}}{2\lambda}\right)m^2T_r^2} e^{j2\pi\left(\frac{a_{0,2}-a_{0,1}}{2\lambda}\right)\left(\frac{f_k}{f_c}\right)m^2T_r^2}\ . \quad (30)$$

As predicted by (30), for different target accelerations, both RM and DFM are compensated for the strongest target while

This article has been accepted for publication in a future issue of this journal, but has not been fully edited. Content may change prior to final publication. Citation information: DOI 10.1109/TAES.2020.3026844, IEEE Transactions on Aerospace and Electronic Systems

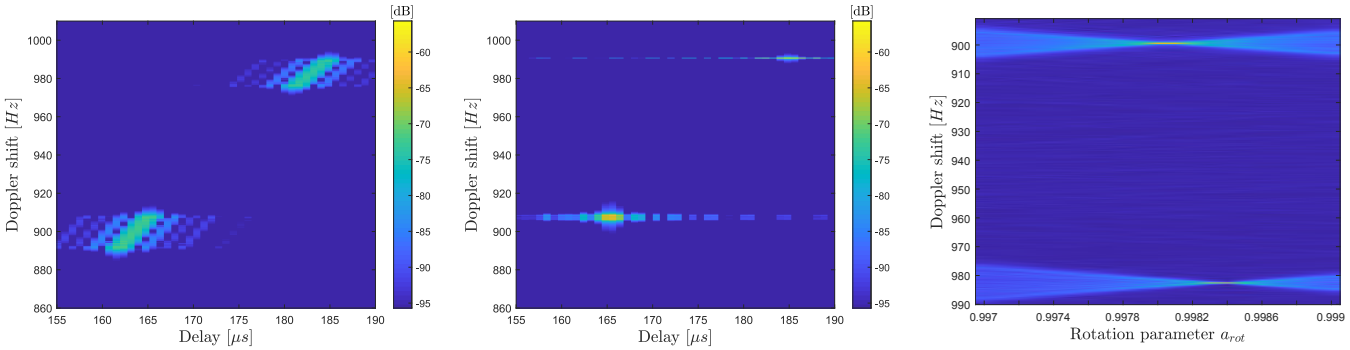

(a) Uncompensated (b) Fully compensated (c) FrFT response

Fig. 5: a) and b) $|\chi_{\text{CAF}}(\tau_H, \nu_H)|^2$ response, c) FrFT response - Simulated geometry, two moving targets, noise-free, T = 4 s

TABLE VII: Two target geometry parameters

Parameter	Value
v_1	211.2975 m/s
v_2	211.539 m/s
$\|\alpha_1\|^2$	-178.84 dB
$\|\alpha_2\|^2$	-176.776 dB
$\tau_{0,1}$	184.97 μs
$\nu_{0,1}$	990.791 Hz
$\tau_{0,2}$	165.39 μs
$\nu_{0,2}$	909.475 Hz

some DFM and quadratic RM remain for the second target. A possible solution is to combine the migration compensation approach with CLEAN-like techniques [38] where Alg. 1 is used to detect the targets iteratively: once the strongest target is detected, its signature is subtracted from the overall response and the residual signal re-processed to compensate and detect the remaining targets. To allow for this however, the target signature model and the parameter estimates should accurately characterize the measured signals. This is rather challenging in our case, particularly due to:

1) Discretized delay and Doppler estimates - the delay discretization is significant due to the narrow LDACS bandwidth, which also limits the separation of closely spaced targets
2) Low chirp rate estimation accuracy for low SNR
3) Lack of amplitude estimates - α_g can be estimated from the maximum peak response, this is however affected by discretization, accuracy, and Batches processing losses.

To address these shortcomings of the non-model based approach, we aim to develop a model-based multi-target scheme which performs joint target detection and parameter estimation while accounting for the migration effects.

V. Super Resolution Sparse Bayesian Learning

The novel model-based approach uses successive interference cancellation. It combines Bayesian estimation and SR-SBL techniques [39]–[41] and imposes sparsity constraints on the number of targets to indirectly account for their detection. Moreover, it delivers not only the target delay, Doppler shift, and acceleration estimates, not restricted to a resolution grid, but also an accurate estimate of the number of targets as well as their weights, addressing all three challenges above.

A. Synthetic Model Simulated Data

The fast-frequency/slow-time model derived in (17) is the starting point for the SBL approach. To assess its suitability in practice, we are interested to compare the responses obtained by processing the FERS radar simulated signal with those using synthetic model-based data. Important to note is the fact that the cross-terms, $X_m(f-\nu_0)$ in (17), are a highly non-linear function of the true target parameters, τ_0 and ν_0 (see Appendix A). Accounting for these dependencies would make the resulting model very complex. As a result, we make the simplifying assumption that, given IID symbols, the segments are uncorrelated and the cross-terms negligible. Also, we assume that, given $\nu_0 \ll B$, $S_m(f_k-\nu_0)S_m^*(f_k) \approx |S_m(f_k)|^2$. The suitability of both of these assumptions will be put to test in Section V-F. The response in (17) is therefore modeled as

$$\mathbf{X}_{\text{ffst}}[k,m] = \alpha e^{-j2\pi f_c \tau_0} |S_m(f_k)|^2 e^{-j2\pi f_k \tau_0} \times e^{j2\pi\nu_0\left(\frac{f_k+f_c}{f_c}\right)mT_r} e^{-j2\pi\frac{a_0}{2\lambda}\left(\frac{f_k+f_c}{f_c}\right)m^2T_r^2} + \Psi_m(f_k)S_m^*(f_k)\ , \quad (31)$$

with α assumed constant across all bins. The model-based uncompensated as well as compensated responses, i.e., using Alg. 1, are shown in Fig. 6 with a noise-free compensated peak response of -55.91 dB. A qualitative assessment allows us to conclude that the model-based responses generally match the non-model based FERS-simulated responses in Fig. 4.

B. Sparse Bayesian Learning Observation Model

Next, we synthesize the SBL observation model. For this, we build on (31) for the multi-target case and assume that the signal is sampled at the bandwidth B and that the segmentation parameters are: $L_{\text{seg}} = 80$, $N_{\text{seg}} = 25000$, and $T_{\max} = 160$. Oversampling is not by default required since the SBL algorithm considered here has SR capabilities. Also, in a real scenario, sampling at the B ensures that the noise samples $\psi(t)$ in the RX remain uncorrelated. Nevertheless, from (31) we note that the noise contribution $\Psi_m(f)S_m^*(f)$ for each segment m is colored. Since colored noise is expected to make the estimation algorithm more complex, we are interested to whiten the noise. This is done by "dividing off" the conjugate spectrum contribution in (31). The resulting observation model, which can be interpreted as directly modeling the FT of the columns of the reshaped reflected signal matrix $\mathbf{R}$, is

This article has been accepted for publication in a future issue of this journal, but has not been fully edited. Content may change prior to final publication. Citation information: DOI 10.1109/TAES.2020.3026844, IEEE Transactions on Aerospace and Electronic Systems

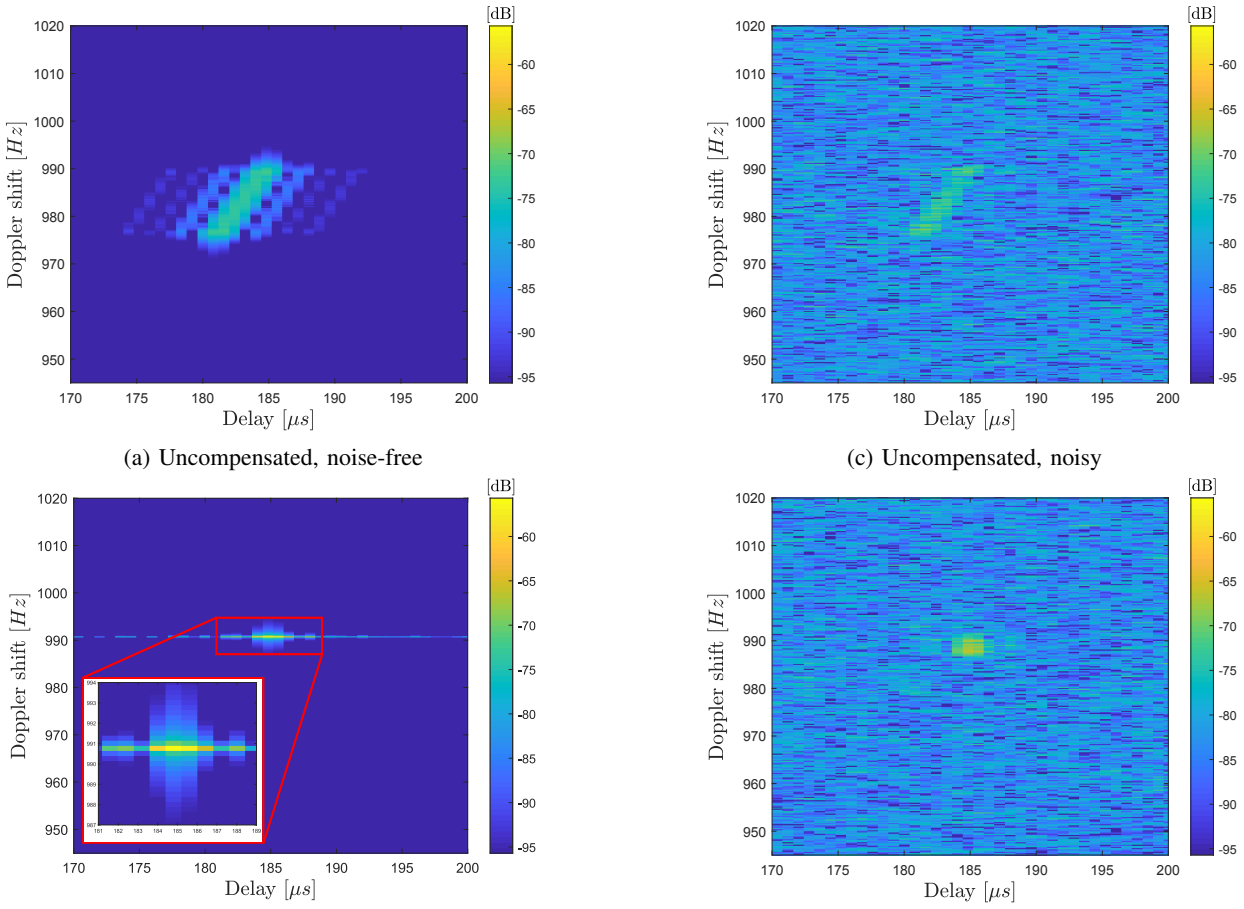

(a) Uncompensated, noise-free

(c) Uncompensated, noisy

(b) Fully compensated - $\widehat{a}_{\text{rot}} = 0.9984$, noise-free

(d) Fully compensated - $\widehat{a}_{\text{rot}} = 0.9988$, noisy

Fig. 6: $\left|\chi_{\text{CAF}}(\tau_H, \nu_H)\right|^2$ - Synthetic model-based Delay-Doppler response, T = 4 s

given as:

$$\underbrace{\mathbf{X}_{\text{ffst}}[k,m]\frac{S_m(f_k)}{|S_m(f_k)|^2}}_{\mathbf{Y}[k,m]} = \sum_{g=1}^{N_g} \underbrace{\alpha_g e^{-j2\pi f_c \tau_{0,g}}}_{w_g} \times \underbrace{S_m(f_k) e^{-j2\pi f_k \tau_{0,g}} e^{j2\pi\nu_{0,g}\left(\frac{f_k+f_c}{f_c}\right)mT_r} e^{-j2\pi\frac{a_{0,g}}{2\lambda}\left(\frac{f_k+f_c}{f_c}\right)m^2T_r^2}}_{\mathbf{A}_g(\boldsymbol{\theta}_g)[k,m]} + \underbrace{\Psi_m(f_k)}_{\widehat{\boldsymbol{\Psi}}[k,m]} \tag{32}$$

$$\mathbf{Y}[k,m] = \mathbf{R}[k,m] = \sum_{g=1}^{N_g} w_g \mathbf{A}_g(\boldsymbol{\theta}_g)[k,m] + \widehat{\boldsymbol{\Psi}}[k,m]. \tag{33}$$

where w_g, $\boldsymbol{\theta}_g$, and $\mathbf{A}_g(\boldsymbol{\theta}_g)$ are the weight, parameter vector, and matrix signature of target g, respectively, while $\widehat{\boldsymbol{\Psi}}$ is the noise matrix. The choice of w_g in (32) ensures that the target weight is complex and constant. Since $S_m(f_k)$ varies along fast-frequency and slow-time it can not be included in w_g. Nevertheless, $S_m(f_k)$ is known, i.e., is a function of the known L_{seg} and N_{seg}, and can thus be part of the target signature. The SBL observation model is expressed in matrix form as:

$$\mathbf{Y}_{K\times M} = \sum_{g=1}^{N_g} w_g \mathbf{A}_g(\boldsymbol{\theta}_g)_{K\times M} + \widehat{\boldsymbol{\Psi}}_{K\times M}\ . \tag{34}$$

Further introducing the vector parameters as the *row-vectorised* version of their matrix counterparts, we formulate the SBL observation model in vector form as

$$\mathbf{y} = \mathbf{X}(\boldsymbol{\theta})\,\mathbf{w} + \widehat{\boldsymbol{\psi}}\ , \tag{35}$$

where $\mathbf{y} = \text{vec}\{\mathbf{Y}\}$, $\mathbf{x}(\boldsymbol{\theta}_g) = \text{vec}\{\mathbf{A}_g(\boldsymbol{\theta}_g)\}$, $\widehat{\boldsymbol{\psi}} = \text{vec}\left\{\widehat{\boldsymbol{\Psi}}\right\}$, $\mathbf{X}(\boldsymbol{\theta}) = \left[\mathbf{x}(\boldsymbol{\theta}_1), \cdots, \mathbf{x}(\boldsymbol{\theta}_{N_g})\right]$, $\boldsymbol{\Theta} = \left[\boldsymbol{\theta}_1, \cdots, \boldsymbol{\theta}_{N_g}\right]$, and $\mathbf{w} = \left[w_1, \cdots, w_{N_g}\right]^T$. The noise $\widehat{\boldsymbol{\psi}}$ is now white circularly symmetric complex Gaussian with zero mean and covariance matrix $\boldsymbol{\Lambda}^{-1} = \sigma^2_{\widehat{\psi}}\mathbf{I}$. Also, $\sigma^2_{\widehat{\psi}}$ models the variance of the FT of the thermal noise samples in the RX. An accurate noise estimate is central to the initialization, since, when the noise level is high, the algorithm is prone to sparsify targets to a larger degree [41]. Here, the noise power is assumed known. In practice, an accurate noise level estimate can be obtained using a CFAR-like approach [42]. Also, given that all the derived expressions account for the general (full) covariance matrix $\boldsymbol{\Lambda}^{-1}$, colored noise or clutter can also be accounted for, albeit at the expense of an increased computational complexity.

C. Bayesian Sparse Modeling

The model in (35) is the starting point for the Bayesian inference approach. Given measured vector $\mathbf{y}$ and known target signature model $\mathbf{X}(\boldsymbol{\theta})$, we aim to detect the number of

targets, N_g, in a sparsely modeled radar scene, and estimate $\boldsymbol{\theta}_g = [\tau_{0,g}, \nu_{0,g}, a_{0,g}]^T$ and w_g for all targets. Within the SBL framework [39], [40], sparsity constraints on $\mathbf{w}$, which indirectly account for target detection, are imposed by using a hierarchical prior distribution such that

$$p(\mathbf{w}|\boldsymbol{\gamma})p(\boldsymbol{\gamma}) = \prod_{g=1}^{N_g} p(w_g|\gamma_g)p(\gamma_g) \ , \tag{36}$$

where γ_g is the sparsity parameter associated with target g. In this work, we employ a Gaussian prior for the weights $p(w_g|\gamma_g) = \mathcal{CN}(w_g|0, \gamma_g)$ and a non-informative prior for the sparsity parameters $p(\gamma_g) \propto \gamma_g^{-1}$. The sparsity is enforced through the use of independent γ_g, which are proportional to the width of the prior PDF allowing one to individually control the contribution associated with each weight w_g. Parameters γ_g are treated as random parameters and need to be estimated. The full posterior distribution to be maximized is therefore

$$p(\mathbf{w}, \boldsymbol{\gamma}, \boldsymbol{\theta}|\mathbf{y}) \propto p(\mathbf{y}|\mathbf{w}, \boldsymbol{\theta}, \boldsymbol{\gamma})p(\mathbf{w}|\boldsymbol{\gamma})p(\boldsymbol{\gamma})p(\boldsymbol{\theta}) \ , \tag{37}$$

however it is not analytically traceable. As a result, we use the variational Bayesian (VB) framework to construct a simpler analytical approximation for (37) and aim to maximize its fit. For this, we adopt the sparse VB space alternating generalized expectation-maximization (VB-SAGE) approach from [41], [43] to our data model in (35). The VB-SAGE is an iterative scheme, which by means of so called *hidden data* permits splitting the multi-dimensional optimization with respect to $\mathbf{w}, \boldsymbol{\gamma}, \boldsymbol{\theta}$ to a sequence of N_g smaller optimizations. As such, N_g potential targets are detected and processed sequentially, significantly reducing the complexity for long CPIs. In the following, we summarize the VB-SAGE steps and the salient estimation expressions associated with updating the g^{th} target parameters based on the available estimates of all the other $N_g - 1$ target components [41], [43]:

1) Hidden data: The hidden data is characterized by the residual signal $\widehat{\mathbf{y}}_g$

$$\widehat{\mathbf{y}}_g = \mathbf{y} - \sum_{h=1, h\neq g}^{N_g} \widehat{w}_h \mathbf{x}(\widehat{\boldsymbol{\theta}}_h) \ , \tag{38}$$

and can be seen as an interference cancellation step which allows us to decouple the targets and only focus on the subset of one single target's parameters at a time. Compared to the CLEAN technique, the approach used here has the advantage of employing non-discretized accurate parameter estimates as well as successively optimizing the parameter estimates of all the targets. The cost function to be optimized is $\mathcal{L}(\boldsymbol{\theta}_g)$:

$$\mathcal{L}(\boldsymbol{\theta}_g) = \log\left|\boldsymbol{\Sigma}_{\widehat{\gamma}_g}(\boldsymbol{\theta}_g)\right| + \mathbf{y}_g^H \boldsymbol{\Sigma}_{\widehat{\gamma}_g}^{-1}(\boldsymbol{\theta}_g)\mathbf{y}_g \ , \text{ where} \tag{39}$$

$$\boldsymbol{\Sigma}_{\widehat{\gamma}_g}(\boldsymbol{\theta}_g) = \boldsymbol{\Lambda}^{-1} + \widehat{\gamma}_g \mathbf{x}(\boldsymbol{\theta}_g)\mathbf{x}(\boldsymbol{\theta}_g)^H \ . \tag{40}$$

2) Target parameter estimation: The estimation of the parameter vector $\boldsymbol{\theta}_g$ reduces then to the following optimization [41]:

$$\widehat{\boldsymbol{\theta}}_g = \arg\min_{\boldsymbol{\theta}_g} \mathcal{L}(\boldsymbol{\theta}_g) \tag{41}$$

Accounting for the non-linear relationship between $\mathbf{x}(\boldsymbol{\theta}_g)$ and the elements of $\boldsymbol{\theta}_g$, i.e., $\tau_{0,g}$, $\nu_{0,g}$, and $a_{0,g}$, the solution to (41) is obtained numerically using gradient-based methods. Appendix B is dedicated to evaluating the two derivatives needed to compute the gradient $\nabla\mathcal{L}(\boldsymbol{\theta}_g)$.

3) Sparsity parameters and signal detection: The sparsity parameter estimation has been shown in [41] to essentially coincide with the target detection procedure. Using the VB framework to estimate $\widehat{\gamma}_g$, the following expression is obtained

$$\widehat{\gamma}_g = \begin{cases} |\mu_g|^2 - \varsigma_g, & |\mu_g|^2/\varsigma_g > \kappa \\ 0, & \text{otherwise} \end{cases} \ , \tag{42}$$

where

$$\mu_g = \varsigma_g \mathbf{x}(\widehat{\boldsymbol{\theta}}_g)^H \boldsymbol{\Lambda} \widehat{\mathbf{y}}_g \ \ , \ \ \varsigma_g = \left(\mathbf{x}(\widehat{\boldsymbol{\theta}}_g)^H \boldsymbol{\Lambda} \mathbf{x}(\widehat{\boldsymbol{\theta}}_g)\right)^{-1} \ . \tag{43}$$

The condition $|\mu_g|^2/\varsigma_g > \kappa$ directly determines if the target at $\widehat{\boldsymbol{\theta}}_g$ remains in the model. Analyzing (42)-(43), $|\mu_g|^2$ represents the absolute value squared of a matched filter response, while $|\mu_g|^2/\varsigma_g$ is the target output SNR, comprising the coherent integration gain. Deciding if the g^{th} target is present is done by comparing the output SNR to the threshold κ, chosen as

$$\kappa = \log\left(KM \frac{\sqrt{\log(KM)}}{\epsilon\sqrt{3/\pi}}\right) , \tag{44}$$

where ϵ is the desired probability of false alarm. The selection of κ arises as a result of the VB-SAGE inference expressions and their relationship to the extremes of the periodogram [44]. This prevents model over-fitting and estimation of artifacts. When the detection condition is not met, $\widehat{\gamma}_g$ is set to zero. This removes the corresponding target contribution and enforces the model sparsity. Furthermore, it can be shown that $\widehat{\gamma}_g$ effectively regularizes the objective function in (41), leading to a stable solution even for closely spaced targets.

4) Weights estimation: Lastly, the weight estimate of the g^{th} target is the mean of the Gaussian weight posterior distribution

$$\widehat{w}_g = \widehat{\Sigma}_w \mathbf{x}(\widehat{\boldsymbol{\theta}}_g)^H \boldsymbol{\Lambda} \widehat{\mathbf{y}}_g \ \text{, where} \tag{45}$$

$$\widehat{\Sigma}_w = \left(\mathbf{x}(\widehat{\boldsymbol{\theta}}_g)^H \boldsymbol{\Lambda} \mathbf{x}(\widehat{\boldsymbol{\theta}}_g) + \widehat{\gamma}_g^{-1}\right)^{-1} \ . \tag{46}$$

D. Iterative Algorithm

The VB-SAGE scheme is presented in Alg. 2 and follows a bottom-up approach. The algorithm starts with an empty model with all estimates set to zero. Search intervals for τ_0, ν_0, and a_0 are defined and the target signature for each parameter combination is evaluated. The initial estimate $\boldsymbol{\theta}'$ is the one that maximizes the fit between the model $\mathbf{x}(\boldsymbol{\theta}')$ and $\mathbf{y}$. If the initial detection condition is met, the target is added to the model, the parameters updated, and the new target weight initialized. Next, a numerical gradient-based optimization using a Broyden, Fletcher, Goldfarb, and Shanno (BFGS) algorithm [45] is used to jointly estimate τ_0, ν_0, and a_0. Then, the sparsity parameter and the weights are estimated. The stopping criterion for updating the parameters is when: i) convergence is achieved, i.e., the maximum change in $\{\boldsymbol{\theta}_g, \gamma_g\}$ between two successive iterations is less than 0.001, or ii) the number of iterations exceeds 30. The estimated signature is then used to obtain the updated residual which is used to initialize new

This article has been accepted for publication in a future issue of this journal, but has not been fully edited. Content may change prior to final publication. Citation information: DOI 10.1109/TAES.2020.3026844, IEEE Transactions on Aerospace and Electronic Systems

targets, until either the detection metric is below κ or the number of targets is too large.

We note here that the algorithm has not yet been optimized for speed. The computational complexity is primarily owed to the SR capability and to the parameter initialization step. In practice, the approach in [46] can be adopted to speed up the former, while the discretized estimates delivered by the migration compensation approach could be used as a-priori information to facilitate the latter.

Algorithm 2 VB-SAGE Algorithm

$\mathbf{X}(\widehat{\boldsymbol{\theta}}) \leftarrow 0, \widehat{\mathbf{w}} \leftarrow 0, \widehat{\boldsymbol{\theta}} \leftarrow \emptyset, \widehat{\mathbf{y}} \leftarrow \emptyset$
Compute κ from (44) using $\epsilon = 0.01$
while Continue adding target **do**
  $\mathbf{r} \leftarrow \mathbf{y} - \mathbf{X}(\widehat{\boldsymbol{\theta}})\widehat{\mathbf{w}}, \quad \boldsymbol{\Psi} \leftarrow \boldsymbol{\Lambda}^{-1} + \sum_{g=1}^{\widehat{N}_g} \widehat{\gamma}_g \mathbf{x}(\widehat{\boldsymbol{\theta}}_g)\mathbf{x}(\widehat{\boldsymbol{\theta}}_g)^H$
  $\boldsymbol{\theta}' \leftarrow \arg\max_{\boldsymbol{\theta}} \left\|\mathbf{r}^H \mathbf{x}(\boldsymbol{\theta})\right\|^2$
  $\varsigma' \leftarrow \left(\mathbf{x}(\boldsymbol{\theta}')^H \boldsymbol{\Psi}^{-1} \mathbf{x}(\boldsymbol{\theta}')\right)^{-1}, \quad \mu' \leftarrow \varsigma' \mathbf{x}(\boldsymbol{\theta}')^H \boldsymbol{\Psi}^{-1} \mathbf{y}$
  if $|\mu'|^2/\varsigma' > \kappa$ **then**
    Add the new target
    $\widehat{N}_g \leftarrow \widehat{N}_g + 1, \ \widehat{\boldsymbol{\theta}}^{[0]} \leftarrow [\widehat{\boldsymbol{\theta}}, \boldsymbol{\theta}'], \ \widehat{\boldsymbol{\gamma}}^{[0]} \leftarrow [\widehat{\boldsymbol{\gamma}}, (|\mu'|^2 - \varsigma')]$
    $\widehat{\mathbf{w}}^{[0]} \leftarrow \left[\widehat{\mathbf{w}}, \frac{\mathbf{x}(\widehat{\boldsymbol{\theta}}_{\widehat{N}_g})^H \mathbf{r}}{\mathbf{x}(\widehat{\boldsymbol{\theta}}_{\widehat{N}_g})^H \mathbf{x}(\widehat{\boldsymbol{\theta}}_{\widehat{N}_g}) + 1/\widehat{\gamma}_{\widehat{N}_g}}\right]$
    while not converged **do**
      for $g = 1 : \widehat{N}_g$ **do**
        Compute residual $\widehat{\mathbf{y}}_g$ from (38)
        Estimate $\widehat{\boldsymbol{\theta}}_g$ numerically from (41) and (40)
        Estimate $\widehat{\gamma}_g$ from (42) using (43)
        Compute $\widehat{w}_g$ from (45) using (46)
      end for
    end while
  else
    Stop adding new targets
  end if
end while

E. Simulation Results and Analysis

To allow for a better understanding of the VB-SAGE scheme we make the following observations:

O1. The algorithm delivers the estimated target weights, delay, Doppler-shift, and acceleration as well the estimated model $\widehat{\mathbf{X}}(\boldsymbol{\theta})$ evaluated at the parameter estimates.
O2. The VB-SAGE estimates account for the RM and DFM and can take values beyond the resolution grid. Also, the choice of $\sigma^2_{\widehat{\psi}}$ ensures that they account for a system noise level equivalent to that of the thermal noise.
O3. The coherent integration gain achieved is inherent to the VB-SAGE estimation algorithm and update expressions.

The core difference between the VB-SAGE and the KT-FrFT approaches is that the former is a model-based while the latter is a non-model based technique. To enable a better comparison between the VB-SAGE algorithm results and the migration compensation ones, we use the VB-SAGE $\widehat{\nu}_0$ and $\widehat{a}_0$ estimates to depict the RM and DFM compensation capabilities when applied to the estimated model $\widehat{\mathbf{X}}(\boldsymbol{\theta})$, which is inherently noise-free. Starting from the relationship between $\widehat{\mathbf{X}}(\boldsymbol{\theta})$ and $\widehat{\mathbf{A}}_g(\boldsymbol{\theta}_g)$ from (35) and (33), a compensated signature can be obtained by "correcting" the RM and DFM effects to obtain

$$\widehat{\mathbf{A}}_g^{\text{comp}}(\boldsymbol{\theta}_g)[k,m] = S_m(f_k) e^{-j2\pi f_k \widehat{\tau}_{0,g}} e^{j2\pi \widehat{\nu}_{0,g} m T_r} , \quad (47)$$

from which the model-compensated response $\widehat{\mathbf{X}}_{\text{ffst}}^{\text{comp}}$ in (22) can be reconstructed as

$$\widehat{\mathbf{X}}_{\text{ffst}}^{\text{comp}}[k,m] = \sum_{g=1}^{N_g} \widehat{w}_g S_m^*(f_k) \widehat{\mathbf{A}}_g^{\text{comp}}(\boldsymbol{\theta}_g)[k,m] . \quad (48)$$

Firstly, we apply the VB-SAGE algorithm to fully synthetic data obtained by parametrizing (33) with the true parameters and adding uncorrelated Gaussian noise with variance $\sigma^2_{\widehat{\psi}}$. We consider the scenario with two well separated targets and use the VB-SAGE estimates to "correct" for the migration effects from the estimated model. The model-compensated delay-Doppler response is shown in Fig. 7a overlaid with the VB-SAGE estimates and true parameters. The estimates, shown as red asterisks, closely match the true parameters, depicted as black circles. We stress that the parameter estimates account for the system noise and that only the compensated model, used here for visualization purposes, is noise-free.

Additionally, we present in Fig. 7b the model-compensated response for a closely spaced scenario: two targets with the same Doppler shift and acceleration and delays spaced closer than the system resolution. The latter do not allow to distinguish between the targets, with Fig. 7b depicting a single peak arising from the interference of the two nearby targets. Overlaying the VB-SAGE estimates on the true parameters nevertheless confirms that the VB-SAGE approach correctly estimates the number of targets and their parameters. Furthermore, it underlines that the algorithm is not only able to separate the two close targets but also does not add any false ones. The VB-SAGE estimates obtained by averaging 50 Monte Carlo simulations are summarized in Table VIII along with the true parameters. Their means can be seen to closely approach the true values, while their standard deviations point to the correspondingly low estimation errors. We also note that in the closely spaced case the delay and weight estimation errors are, as expected, slightly larger than in the well separated scenario.

F. Model Mismatch Sources

Having confirmed the performance of the VB-SAGE approach when using synthetic data, we present three sources of model mismatch that can occur when using radar data:

M1. The true target signature differs from the model.
M2. The noise samples are partially correlated.
M3. The propagation loss α_g varies greatly during the CPI.

A model mismatch can reduce the estimation accuracy and bring along a residual error which can trigger the introduction of false targets with very small weights. We are interested to analyze the extent to which the estimation routine may be impacted as a result.

Let us begin with M1. The reshaping procedure used to obtain (17) gives rise to cross-contributions. A non-linear function of the true unknown $\tau_{0,g}$ and $\nu_{0,g}$, these are currently not

This article has been accepted for publication in a future issue of this journal, but has not been fully edited. Content may change prior to final publication. Citation information: DOI 10.1109/TAES.2020.3026844, IEEE Transactions on Aerospace and Electronic Systems

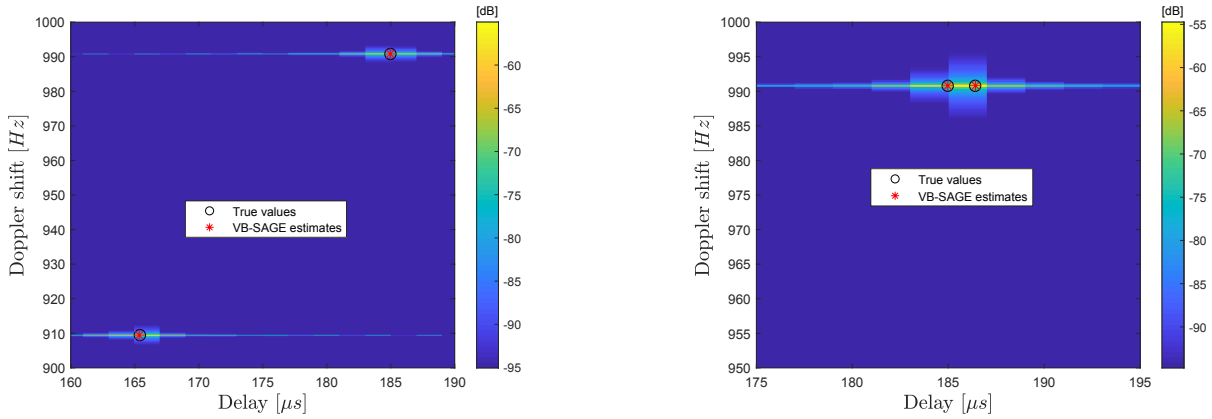

(a) Two well separated targets

(b) Two closely spaced targets

Fig. 7: $|\chi_{\text{CAF}}(\tau_H, \nu_H)|^2$ - VB-SAGE model-compensated Delay-Doppler response, fully synthetic, T = 4 s

TABLE VIII: VB-SAGE estimates - fully synthetic model, averaged over 50 Monte Carlo runs

Scenario	Target	True/Estimated parameters							
		$\tau_{0,g}$ (μs)	$\widehat{\tau}_{0,g}$ (μs)	$\nu_{0,g}$ (Hz)	$\widehat{\nu}_{0,g}$ (Hz)	$a_{0,g}$ (m/s^2)	$\widehat{a}_{0,g}$ (m/s^2)	α_g^2 (dB)	$\lvert\widehat{w}_g\rvert^2$ (dB)
Closely spaced	1	184.97	184.975 $\pm$ 0.059	990.791	990.790 $\pm$ 0.012	1.2118	1.2117 $\pm$ 0.0017	-178.848	-178.851 $\pm$ 0.31
	2	186.4	186.391 $\pm$ 0.054	990.791	990.791 $\pm$ 0.013	1.2118	1.2116 $\pm$ 0.0020	-178.848	-178.782 $\pm$ 0.25
Well separated	1	184.97	184.965 $\pm$ 0.022	990.791	990.791 $\pm$ 0.014	1.2118	1.2118 $\pm$ 0.0022	-178.848	-178.873 $\pm$ 0.24
	2	165.39	165.388 $\pm$ 0.019	909.475	909.476 $\pm$ 0.010	1.439	1.4392 $\pm$ 0.0015	-176.776	-176.785 $\pm$ 0.14

accounted for in (32). Also, the Doppler shift of the fast-time spectrum, shown in (17), is also not accounted for. The target signature model in (32) is therefore accurate only if: i) $X_m(f-\nu_0)$ is negligible and ii) $S_m(f-\nu_0) \approx S_m(f)$.

An initial assessment has confirmed that, even for IID symbols, the cross-contributions can not be assumed negligible and do result in a model mismatch when using radar simulated data. Although difficult to model analytically, these cross-contributions can be taken into account numerically. To confirm this we have applied the VB-SAGE algorithm to FERS radar simulated data while using an updated observation model in which the cross-contributions are modeled exactly as in (50) using the true target parameters. Preliminary results delivered high accuracy estimates and did not introduce any false targets. As such, M1 can be eliminated by an appropriate extension of the observation model, and remains the topic of future work.

Now, let us consider M2. In (35) it is assumed that the noise samples are uncorrelated and Gaussian distributed. In reality, the zero-padding underlying the FT operation introduces some correlation among the noise samples, the extent of which is partially dispersed by the row-vectorization operation used to obtain (35) from (34). To assess the impact of the leftover correlation, we employ partially synthetic data in which the noise contribution is recreated according to the steps that would be applied in practice to the radar data. These are:

- Generate Gaussian vector of dimension $L_{\text{seg}} \times N_{\text{seg}} + L_{\max}$ and variance σ_ψ^2
- Perform signal segmentation with $L_{\max}$ samples overlap
- Take column-wise FT of the noise matrix: $N_{\text{FFT,ft}} = 2^{\text{nextpow2}(2\times L_{\text{seg}}+L_{\max}-1)}$.

The resulting row-vectorized "whitened" noise vector is added to the target signature to generate the observed signal $\mathbf{y}$. This allows us to decouple the model mismatch sources and assess solely the impact of the partially correlated noise samples (M2) on the estimation performance. The resulting estimates are presented in Table IX and can be compared to the ones in Table VIII corresponding to a fully synthetic model. Also, the associated model-compensated responses are shown in Fig. 8. We observe that for the two closely spaced targets in Fig. 8b the model order, i.e., number of targets, is correctly estimated. The accuracy of the estimates, in particular of the delay, is slightly reduced when compared to the fully synthetic case, while $|\widehat{w}_g|^2$ are slightly larger than the true α_g^2.

Comparatively, for the well separated case in Fig. 8a, the estimates closely approach the true $\tau_{0,g}, \nu_{0,g}, a_{0,g}$ although $|\widehat{w}_g|^2$ is estimated to be smaller than the ground truth. The latter leads to the introduction of a third target with a very small weight. The detection condition is only borderline met for this false target since $|\mu_3|^2/\varsigma_3$ is only slightly larger than κ. Decreasing ϵ, would increase the threshold κ and correctly prevent the introduction of this artifact. Indeed, simulations show that for $\epsilon = 0.001$, only the actual targets are detected.

Alternatively, we can reduce the FFT size to $N_{\text{FFT,ft2}} = 2^{\text{nextpow2}(L_{\text{seg}}+L_{\max}-1)}$. $N_{\text{FFT,ft}}$ is needed to ensure that the frequency domain fast-time circular correlation maps to a linear correlation in time domain. Nevertheless, only the first $L_{\max}$ fast-time bin samples, corresponding to $\tau_{\max}$, are kept after returning to time domain. Using the reduced $N_{\text{FFT,ft2}}$ still ensures a linear correlation for the first $L_{\max}$ bins. For the case considered here, using $N_{\text{FFT,ft2}} = 256$ instead of $N_{\text{FFT,ft}} = 512$ drastically decreases the amount of zero-padding and minimizes the noise samples correlation. Simulations confirm our intuition, with the results obtained for $N_{\text{FFT,ft2}} = 256$ shown in the first row of Table X for the constant α_g case and the original $\epsilon = 0.01$. As one can see, only the true targets are detected and no artifacts are introduced.

This article has been accepted for publication in a future issue of this journal, but has not been fully edited. Content may change prior to final publication. Citation information: DOI 10.1109/TAES.2020.3026844, IEEE Transactions on Aerospace and Electronic Systems

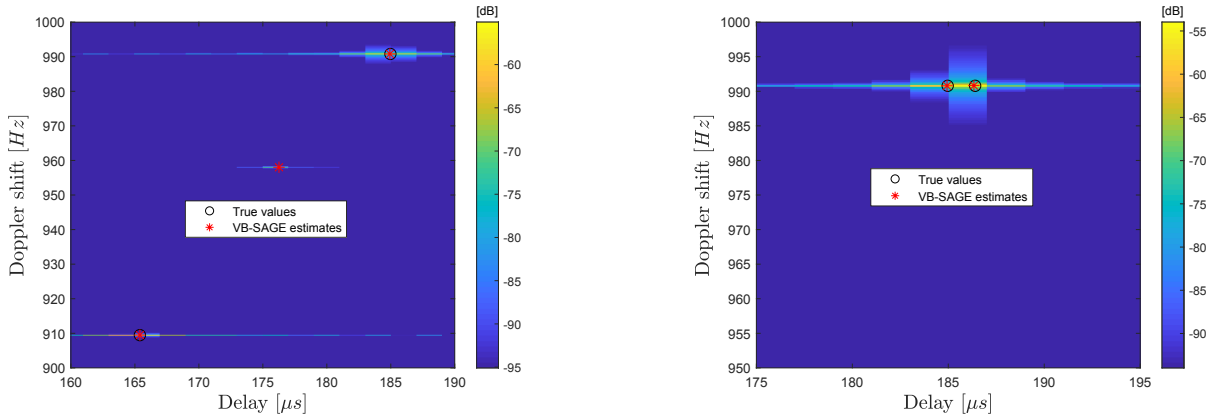

(a) Two well separated targets

(b) Two closely spaced targets

Fig. 8: $|\chi_{\text{CAF}}(\tau_H, \nu_H)|^2$ - VB-SAGE model-compensated Delay-Doppler response, partially synthetic, T = 4 s

TABLE IX: VB-SAGE estimates - partially synthetic model

Scenario	Target	True/Estimated parameters							
		$\tau_{0,g}$ (μs)	$\widehat{\tau}_{0,g}$ (μs)	$\nu_{0,g}$ (Hz)	$\widehat{\nu}_{0,g}$ (Hz)	$a_{0,g}$ (m/s^2)	$\widehat{a}_{0,g}$ (m/s^2)	α_g^2 (dB)	$\lvert\widehat{w}_g\rvert^2$ (dB)
Closely spaced	1	184.97	184.93	990.791	990.7939	1.2118	1.2120	-178.848	-178.4485
	2	186.4	186.34	990.791	990.8196	1.2118	1.2165	-178.848	-178.2217
Well separated	1	184.97	184.93	990.791	990.7972	1.2118	1.2124	-178.848	-178.4622
	2	165.39	165.39	909.475	909.4924	1.439	1.4411	-176.776	-177.1232
	3	-	176.26	-	958.0301	-	1.1022	-	-194.1548

TABLE X: VB-SAGE estimates - partially synthetic model, reduced zero-padding

Scenario	Target	True/Estimated parameters							
		$\tau_{0,g}$ (μs)	$\widehat{\tau}_{0,g}$	$\nu_{0,g}$ (Hz)	$\widehat{\nu}_{0,g}$	$a_{0,g}$ (m/s^2)	$\widehat{a}_{0,g}$	α_g^2 (dB)	$\lvert\widehat{w}_g\rvert^2$ (dB)
Well separated α_g constant	1	184.97	184.93	990.791	990.7966	1.2118	1.2124	-178.848	-178.4742
	2	165.39	165.39	909.475	909.4923	1.439	1.4411	-176.776	-177.1350
Well separated α_g variations	1	184.97	184.93	990.791	990.7966	1.2118	1.2124	[-178.45,-178.85]	-178.2811
	2	165.39	165.39	909.475	909.4921	1.439	1.4410	[-176.34,-176.78]	-176.9077

Finally, we consider M3 and note that α_g, so far assumed constant, can vary during the CPI due to the target movement. Given that VB-SAGE expects a constant w_g, M3 can be of concern for scenarios with large variations in α_g. To assess its impact, we consider the joint effect of M2 and M3, i.e., partially correlated noise samples with reduced zero-padding and α_g variations during the CPI. To reproduce the slow-time variation in α_g, we interpolate between the true target position at the start and end of the CPI to obtain α_g at the beginning of each segment. For the velocities considered here, characteristic of typical commercial aircraft, α_g^2 varies as given in the second row of Table X. These varying weights are multiplied with the target signature and combined with the partially-correlated noise samples to generate the observed signal. Applying the VB-SAGE to this scenario we obtain the results summarized in Table X. Although both M2 and M3 are included in the synthetic simulated data, the estimation accuracy remains good, and no false targets are added.

VI. Conclusions

In this work, we investigated the limitations that the RM and DFM impose when using a long CPI to integrate the LDACS reflected signals. Motivated by the large impact of the DFM even for non-accelerating targets, we combined the state-of-the-art KT and FrFT techniques to jointly compensate for both RM and DFM. The results showed that if the geometry-induced acceleration is accurately estimated, the migration effects can be compensated and the target energy refocused. Nevertheless, for low input SNR conditions specific to a passive radar operation, estimating the small acceleration using the FrFT has a reduced accuracy and results in an imperfect DFM compensation, preventing a coherent SNR increase. Additionally, this approach suffers from discretization losses and does not have SR capabilities. The latter is particularly crucial in our case due to the narrow LDACS bandwidth.

Moreover, we have shown that the coupling of the migration effects and the superposition of multiple chirps in multi-target scenarios prevent applying this non-model based approach for the simultaneous compensation of RM and DFM of all targets. Furthermore, the reduced accuracy and discretized parameter estimates as well as the lack of amplitude estimates pose additional challenges for alternative CLEAN-like implementations.

To address all these shortcomings, we proposed a novel model-based SR-SBL estimation technique. For this, we synthesized a multi-target observation model which accurately depicts the RM and DFM effects and used the VB-SAGE algorithm

to perform joint target detection and parameter estimation whilst employing long CPIs. In the proposed approach, which implements a successive interference cancellation that goes beyond CLEAN, the migration effects are accounted for in the observation model employed for the SR estimation algorithm. Additionally, the target weights are also estimated. The results obtained using synthetic data accurately represent the radar scene of interest in terms of the number of targets and their parameters. Also, the absolute values of the complex target weights closely match the propagation loss factors. Regarding the use of this approach with radar data, three possible sources of model mismatch were identified: 1) target signature model mismatch, 2) correlated noise samples, and 3) propagation loss variations. Our analysis has shown that the third has a negligible impact for realistic target movements, while the impact of the second can be significantly reduced by using a row-vectorized operation and reducing the FT size. Comparatively, the first source can can have a rather large impact in practice. Indeed, a target signature model mismatch may arise due to the cross-contributions originating from the reshaping process underlying the Batches processing. These cross-contributions are not easily analytically traceable and therefore currently not accounted for in the target signature model. A preliminary assessment has nevertheless confirmed that the cross-contributions can be taken into account numerically and that this source of model mismatch can be eliminated in future work by a proper extension of the observation model.

APPENDIX A

Signal $r_m(t')$ consists of a delayed version of the segment of interest $s_m(t')$ as well as of cross-contributions. The cross-contributions arise from neighboring segments $s_{m-m_l}(t')$ and $s_{m+m_r}(t')$, where m_l (m_r) are the indices to the left (right) of slow-time index m, the contents of which are partially of completely found in $r_m(t')$. Accounting for these contributions we rewrite (16) in the form given in (49), where $L_{m,a}$ and $L_{\max}$ are the number of samples in the target delay in the m^{th} segment and in $\tau_{\max}$. Assuming that L_{seg} is chosen such that the target range and velocity are constant within a segment while the acceleration-induced phase change is negligible, (49) can be further simplified as given in (50). Using the Parseval theorem we obtain (51) as a fast-frequency domain equivalent of (50), which is further simplified as in (52). The quantities $S^{p_l}_{m-m_l}(f)$ and $S^{p_r}_{m+m_r}(f)$ are the FT of the adjacent segment contributions in the m^{th} segment. The number of these cross-contributions as well as their size are both a function of L_{seg}, $L_{\max}$, and $L_{m,a}$. Realistically assuming that $f_c - \nu_0 \approx f_c$ and $\nu_0^2 \ll f_c$ allows to simplify (52) further as specified in (17).

APPENDIX B

Using the identity $\text{Trace}(\mathbf{ABC}) = \text{Trace}(\mathbf{CAB})$ the derivative of the log term in (41) is given in (53). Also, the derivative of the quadratic term in (41) is shown in (54) while the combined cost function gradient in (55). Using the matrix inversion lemma we express

$$\boldsymbol{\Sigma}^{-1}_{\widehat{\gamma}_g}(\boldsymbol{\theta}_g) = \boldsymbol{\Lambda} - \frac{1}{1/\widehat{\gamma}_g + \mathbf{x}(\boldsymbol{\theta}_g)^H \boldsymbol{\Lambda} \mathbf{x}(\boldsymbol{\theta}_g)} \boldsymbol{\Lambda}\mathbf{x}(\boldsymbol{\theta}_g)\mathbf{x}(\boldsymbol{\theta}_g)^H \boldsymbol{\Lambda} \,. \tag{57}$$

Substituting (57) in (55) and computing the analytical derivatives of $\mathbf{x}(\boldsymbol{\theta}_g)$ with respect to $\theta_{g,1} \equiv \tau_{0,g}$, $\theta_{g,2} \equiv \nu_{0,g}$, and $\theta_{g,3} \equiv a_{0,g}$, the parameters can be numerically estimated.

ACKNOWLEDGMENT

The authors would like to thank Prof. Dr. Daniel O'Hagan and the Radar Remote Sensing Group members at the University of Cape Town for the support provided to set up the FERS radar simulator. FERS was used in this work to generate the LDACS bistatic radar reflected signals.

REFERENCES

[1] R. Perry *et al.*, "SAR imaging of moving targets," *IEEE Trans. on Aerospace and Electronic Systems*, vol. 35, no. 1, 1999.

[2] M. A. Richards, "The keystone transformation for correcting range migration in range-doppler processing," 2014.

[3] X. Chen *et al.*, "Maneuvering target detection via Radon-fractional Fourier transform-based long-time coherent integration," *IEEE Transactions on Signal Processing*, vol. 62, no. 4, pp. 939–953, 2014.

[4] X. Li *et al.*, "A fast maneuvering target motion parameters estimation algorithm based on ACCF," *IEEE Signal Processing Letters*, vol. 22, no. 3, pp. 270–274, 2014.

[5] X. Li *et al.*, "Range Migration Correction for Maneuvering Target based on Generalized Keystone Transform," in *IEEE Radar Conference*, 2015.

[6] X. Li *et al.*, "Coherent integration for maneuvering target detection based on Radon-Lv's distribution," *IEEE Signal Processing Letters*, vol. 22, no. 9, pp. 1467–1471, 2015.

[7] P. Huang *et al.*, "Long-time coherent integration for weak maneuvering target detection and high-order motion parameter estimation based on keystone transform," *IEEE Transactions on Signal Processing*, vol. 64, no. 15, 2016.

[8] Y. Feng *et al.*, "The migration compensation methods for DTV based passive radar," in *IEEE Radar Conference*, 2013.

[9] X. Guan *et al.*, "An extended processing scheme for coherent integration and parameter estimation based on matched filtering in passive radar," *Journal of Zhejiang University*, 2014.

[10] K. M. Scott *et al.*, "The Keystone transform: practical limits and extension to second order corrections," in *IEEE Radar Conference*, 2015.

[11] T. Shan *et al.*, "Efficient architecture and hardware implementation of coherent integration processor for digital video broadcast-based passive bistatic radar," *IET Radar, Sonar & Navigation*, vol. 10, no. 1, 2016.

[12] X. Bai *et al.*, "A processing scheme for long integration time passive radar based on CZT and FRFD-sharpness," in *IEEE International Conference on Signal Processing, Communications and Computing*, 2016.

[13] Z. Li *et al.*, "Multi-frame fractional Fourier transform technique for moving target detection with space-based passive radar," *IET Radar, Sonar & Navigation*, vol. 11, no. 5, pp. 822–828, 2016.

[14] F. Pignol *et al.*, "Lagrange polynomial interpolation based Keystone Transform for passive radar," *IEEE Trans. on Aerospace and Electronic Systems*, 2017.

[15] L. Liu *et al.*, "The CAF-DFRFT-KT algorithm for high-speed target detection in passive radar," in *First International Conference on Instrumentation, Measurement, Computer, Communication and Control*, 2011.

[16] T. Hoshino *et al.*, "Long-time integration by short-time cross-correlation and two-step doppler processing for passive bistatic radar," in *2013 European Radar Conference*, 2013.

[17] S. Subedi *et al.*, "Motion parameter estimation of multiple ground moving targets in multi-static passive radar systems," *EURASIP Journal on Advances in Signal Processing*, vol. 2014, no. 1, p. 157, 2014.

This article has been accepted for publication in a future issue of this journal, but has not been fully edited. Content may change prior to final publication. Citation information: DOI 10.1109/TAES.2020.3026844, IEEE Transactions on Aerospace and Electronic Systems

$$\mathbf{X}_{\text{ftst}}(t',m)=\sum_{m_l=1}^{\lceil L_{m,a}/L_{\text{seg}}\rceil}\int_0^{\tau_a(t)}\alpha s_{m-m_l}\left(y-\left[\left(\tau_0-\frac{\nu_0}{f_c}(y+mT_r)+\frac{a_0}{2c}(y+mT_r)^2\right)-m_lT_r\right]\right)e^{-j2\pi f_c\left(\tau_0-\frac{\nu_0}{f_c}(y+mT_r)+\frac{a_0}{2c}(y+mT_r)^2\right)}s_m^*(y-t')dy$$
$$+\sum_{m_r=1}^{\lceil (L_{\max}-L_{m,a})/L_{\text{seg}}\rceil}\int_{\tau_a(t)+T_r}^{T_r+\tau_{\max}}\alpha s_{m+m_r}\left(y-\left[\left(\tau_0-\frac{\nu_0}{f_c}(y+mT_r)+\frac{a_0}{2c}(y+mT_r)^2\right)+m_rT_r\right]\right)e^{-j2\pi f_c\left(\tau_0-\frac{\nu_0}{f_c}(y+mT_r)+\frac{a_0}{2c}(y+mT_r)^2\right)}s_m^*(y-t')dy$$
$$+\int_{\tau_a(t)}^{\tau_a(t)+T_r}\alpha s_m\left(y-\left(\tau_0-\frac{\nu_0}{f_c}(y+mT_r)+\frac{a_0}{2c}(y+mT_r)^2\right)\right)e^{-j2\pi f_c\left(\tau_0-\frac{\nu_0}{f_c}(y+mT_r)+\frac{a_0}{2c}(y+mT_r)^2\right)}s_m^*(y-t')dy+\int_{-\infty}^{\infty}\psi_m(y)s_m^*(y-t')dy \tag{49}$$

$$\mathbf{X}_{\text{ftst}}(t',m)=\alpha e^{-j2\pi f_c\tau_0}e^{j2\pi\nu_0mT_r}e^{-j2\pi f_c\frac{a_0}{2c}(mT_r)^2}\times$$
$$\left[\sum_{m_l=1}^{\lceil L_{m,a}/L_{\text{seg}}\rceil}\int_0^{\tau_a(t)}s_{m-m_l}\left(y-\left[\underbrace{\left(\tau_0-\frac{\nu_0}{f_c}(mT_r)+\frac{a_0}{2c}(mT_r)^2\right)}_{\tau_a(mT_r)}-m_lT_r\right]\right)e^{j2\pi\nu_0y}s_m^*(y-t')dy\right.$$
$$+\sum_{m_r=1}^{\lceil (L_{\max}-L_{m,a})/L_{\text{seg}}\rceil}\int_{\tau_a(t)+T_r}^{T_r+\tau_{\max}}\alpha s_{m+m_r}\left(y-\left[\left(\tau_0-\frac{\nu_0}{f_c}(mT_r)+\frac{a_0}{2c}(mT_r)^2\right)+m_rT_r\right]\right)e^{j2\pi\nu_0y}s_m^*(y-t')dy$$
$$\left.+\int_{\tau_a(t)}^{\tau_a(t)+T_r}\alpha s_m\left(y-\left(\tau_0-\frac{\nu_0}{f_c}(mT_r)+\frac{a_0}{2c}(mT_r)^2\right)\right)e^{j2\pi\nu_0y}s_m^*(y-t')dy\right]+\int_{-\infty}^{\infty}\psi_m(y)s_m^*(y-t')dy \tag{50}$$

$$\mathbf{X}_{\text{ffst}}(f,m)=\alpha e^{-j2\pi f_c\tau_0}e^{j2\pi\nu_0\tau_0}\left[\sum_{m_l=1}^{\lceil L_{m,a}/L_{\text{seg}}\rceil}S_{m-m_l}^{p_l}(f-\nu_0)S_m^*(f)e^{j2\pi\nu_0mT_r}e^{-j2\pi f_c\frac{a_0}{2c}(mT_r)^2}e^{-j2\pi(\tau_a(mT_r)-m_lT_r)(f-\nu_0)}\right.$$
$$+\sum_{m_r=1}^{\lceil (L_{\max}-L_{m,a})/L_{\text{seg}}\rceil}S_{m+m_r}^{p_r}(f-\nu_0)S_m^*(f)e^{j2\pi\nu_0mT_r}e^{-j2\pi f_c\frac{a_0}{2c}(mT_r)^2}e^{-j2\pi(\tau_a(mT_r)+m_rT_r)(f-\nu_0)}$$
$$\left.+S_m(f-\nu_0)S_m^*(f)e^{j2\pi\nu_0mT_r}e^{-j2\pi f_c\frac{a_0}{2c}(mT_r)^2}e^{-j2\pi\tau_a(mT_r)(f-\nu_0)}\right]+\Psi_m(f)S_m^*(f) \tag{51}$$

$$\mathbf{X}_{\text{ffst}}(f,m)=\alpha\left[\underbrace{\sum_{m_l=1}^{\lceil L_{m,a}/L_{\text{seg}}\rceil}S_{m-m_l}^{p_l}(f-\nu_0)e^{j2\pi(f-\nu_0)m_lT_r}+\sum_{m_r=1}^{\lceil (L_{\max}-L_{m,a})/L_{\text{seg}}\rceil}S_{m+m_r}^{p_r}(f-\nu_0)e^{-j2\pi(f-\nu_0)m_rT_r}}_{X_m(f-\nu_0)\,=\,\text{cross-terms}}+S_m(f-\nu_0)\right]$$
$$\times S_m^*(f)e^{-j2\pi(f_c-\nu_0)\tau_0}e^{-j2\pi f\tau_0}e^{j2\pi\nu_0mT_r}e^{j2\pi\nu_0\frac{f}{f_c}mT_r}e^{j2\pi\frac{\nu_0^2}{f_c}mT_r}e^{-j2\pi(f_c-\nu_0)\frac{a_0}{2c}(mT_r)^2}e^{-j2\pi f\frac{a_0}{2c}(mT_r)^2}+S_m^*(f)\Psi_m(f)\,. \tag{52}$$

$$\frac{\partial}{\partial\theta_{g,i}}\left(\log\left|\mathbf{\Sigma}_{\widehat{\gamma}_g}(\boldsymbol{\theta}_g)\right|\right)=\text{Trace}\left(\mathbf{\Sigma}_{\widehat{\gamma}_g}^{-1}(\boldsymbol{\theta}_g)\frac{\partial\mathbf{\Sigma}_{\widehat{\gamma}_g}(\boldsymbol{\theta}_g)}{\partial\theta_{g,i}}\right)=\widehat{\gamma}_g\text{Trace}\left(\mathbf{\Sigma}_{\widehat{\gamma}_g}^{-1}(\boldsymbol{\theta}_g)\left(\frac{\partial\mathbf{x}(\boldsymbol{\theta}_g)}{\partial\theta_{g,i}}\mathbf{x}(\boldsymbol{\theta}_g)^H+\mathbf{x}(\boldsymbol{\theta}_g)\frac{\partial\mathbf{x}(\boldsymbol{\theta}_g)^H}{\partial\theta_{g,i}}\right)\right) \tag{53}$$
$$=\widehat{\gamma}_g\left[\text{Trace}\left(\underbrace{\mathbf{x}(\boldsymbol{\theta}_g)^H\mathbf{\Sigma}_{\widehat{\gamma}_g}^{-1}(\boldsymbol{\theta}_g)\frac{\partial\mathbf{x}(\boldsymbol{\theta}_g)}{\partial\theta_{g,i}}}_{\text{scalar}}\right)+\text{Trace}\left(\underbrace{\frac{\partial\mathbf{x}(\boldsymbol{\theta}_g)^H}{\partial\theta_{g,i}}\mathbf{\Sigma}_{\widehat{\gamma}_g}^{-1}(\boldsymbol{\theta}_g)\mathbf{x}(\boldsymbol{\theta}_g)}_{\text{scalar}}\right)\right]=\widehat{\gamma}_g\left[\mathbf{x}(\boldsymbol{\theta}_g)^H\mathbf{\Sigma}_{\widehat{\gamma}_g}^{-1}(\boldsymbol{\theta}_g)\frac{\partial\mathbf{x}(\boldsymbol{\theta}_g)}{\partial\theta_{g,i}}+\frac{\partial\mathbf{x}(\boldsymbol{\theta}_g)^H}{\partial\theta_{g,i}}\mathbf{\Sigma}_{\widehat{\gamma}_g}^{-1}(\boldsymbol{\theta}_g)\mathbf{x}(\boldsymbol{\theta}_g)\right]$$
$$\frac{\partial\widehat{\mathbf{y}}_g^H\mathbf{\Sigma}_{\widehat{\gamma}_g}^{-1}(\boldsymbol{\theta}_g)\widehat{\mathbf{y}}_g}{\partial\theta_{g,i}}=\widehat{\mathbf{y}}_g^H\left(\frac{\partial\mathbf{\Sigma}_{\widehat{\gamma}_g}^{-1}(\boldsymbol{\theta}_g)}{\partial\theta_{g,i}}\right)\widehat{\mathbf{y}}_g=\widehat{\mathbf{y}}_g^H\left(-\mathbf{\Sigma}_{\widehat{\gamma}_g}^{-1}(\boldsymbol{\theta}_g)\frac{\partial\mathbf{\Sigma}_{\widehat{\gamma}_g}(\boldsymbol{\theta}_g)}{\partial\theta_{g,i}}\mathbf{\Sigma}_{\widehat{\gamma}_g}^{-1}(\boldsymbol{\theta}_g)\right)\widehat{\mathbf{y}}_g$$
$$=-\widehat{\gamma}_g\widehat{\mathbf{y}}_g^H\mathbf{\Sigma}_{\widehat{\gamma}_g}^{-1}(\boldsymbol{\theta}_g)\left(\frac{\partial\mathbf{x}(\boldsymbol{\theta}_g)}{\partial\theta_{g,i}}\mathbf{x}(\boldsymbol{\theta}_g)^H+\mathbf{x}(\boldsymbol{\theta}_g)\frac{\partial\mathbf{x}(\boldsymbol{\theta}_g)^H}{\partial\theta_{g,i}}\right)\mathbf{\Sigma}_{\widehat{\gamma}_g}^{-1}(\boldsymbol{\theta}_g)\widehat{\mathbf{y}}_g \tag{54}$$
$$\frac{\partial\mathcal{L}(\boldsymbol{\theta}_g)}{\partial\theta_{g,i}}=\widehat{\gamma}_g\left(\mathbf{x}(\boldsymbol{\theta}_g)^H\mathbf{\Sigma}_{\widehat{\gamma}_g}^{-1}(\boldsymbol{\theta}_g)\frac{\partial\mathbf{x}(\boldsymbol{\theta}_g)}{\partial\theta_{g,i}}+\frac{\partial\mathbf{x}(\boldsymbol{\theta}_g)^H}{\partial\theta_{g,i}}\mathbf{\Sigma}_{\widehat{\gamma}_g}^{-1}(\boldsymbol{\theta}_g)\mathbf{x}(\boldsymbol{\theta}_g)-\widehat{\mathbf{y}}_g^H\mathbf{\Sigma}_{\widehat{\gamma}_g}^{-1}(\boldsymbol{\theta}_t)\frac{\partial\mathbf{x}(\boldsymbol{\theta}_g)}{\partial\theta_{g,i}}\mathbf{x}(\boldsymbol{\theta}_g)^H\mathbf{\Sigma}_{\widehat{\gamma}_g}^{-1}(\boldsymbol{\theta}_g)\widehat{\mathbf{y}}_g\right.$$
$$\left.-\widehat{\mathbf{y}}_g^H\mathbf{\Sigma}_{\widehat{\gamma}_g}^{-1}(\boldsymbol{\theta}_g)\mathbf{x}(\boldsymbol{\theta}_g)\frac{\partial\mathbf{x}(\boldsymbol{\theta}_g)^H}{\partial\theta_{g,i}}\mathbf{\Sigma}_{\widehat{\gamma}_g}^{-1}(\boldsymbol{\theta}_g)\widehat{\mathbf{y}}_g\right)\,. \tag{55}$$

[18] H.-B. Sun *et al.*, "Application of the Fractional Fourier transform to moving target detection in airborne SAR," *IEEE Trans. on Aerospace and Electronic Systems*, vol. 38, no. 4, 2002.

[19] J. Tian *et al.*, "A novel method for parameter estimation of space moving targets," *IEEE Geoscience and Remote Sensing Letters*, vol. 11, no. 2, 2013.

[20] X. Li *et al.*, "A low complexity coherent integration method for maneuvering target detection," *Digital Signal Processing*, vol. 49, 2016.

[21] A. Filip-Dhaubhadel, "L-Band Digital Aeronautical Communication System (LDACS) - Based Non-Cooperative Passive Multistatic Radar for Civil Aviation Surveillance," PhD thesis, Technische Universität Chemnitz, 2020, to be published.

[22] A. Filip *et al.*, "Sparse bayesian learning for long coherent integration time in passive radar systems," in *IET International Conference on Radar Systems*, 2017.

[23] S. Bidon *et al.*, "Bayesian sparse estimation of migrating targets for wideband radar," *IEEE Trans. on Aerospace and Electronic Systems*, vol. 50, no. 2, 2014.

[24] Eurocontrol, "The LDACS1 Prototype Specifications (D3 Deliverable)," 2009.

[25] F. Le Chevalier, *Principles of radar and sonar signal processing*. Artech House, 2002.

[26] A. W. Rihaczek, *Principles of High-Resolution Radar*. 1996.

[27] C. Moscardini *et al.*, "Batches Algorithm for Passive Radar: A Theoretical Analysis," *IEEE Trans. on Aerospace and Electronic Systems*, vol. 51, no. 2, pp. 1475–1487, 2015.

[28] M. Brooker, "The design and implementation of a simulator for multistatic radar systems," PhD thesis, University of Cape Town, 2008.

[29] UCT Radar Remote Sensing Group. (2018). FERS - Flexible, Extensible Radar and Sonar Simulator.

[30] L. Rabiner *et al.*, "The chirp z-transform algorithm," *IEEE Trans. on Audio and Electroacoustics*, vol. 17, no. 2, 1969.

[31] R. Melino and H.-T. Tran, "Application of the Fractional Fourier Tansform in the detection of accelerating targets in clutter," DSTO, Tech. Rep., 2011.

[32] H.-T. Tran and R. Melino, "Application of the Fractional Fourier Transform and S-method in doppler radar tomography," DSTO, Tech. Rep., 2010.

[33] H.-T. Tran *et al.*, "Detection of accelerating targets in clutter using a de-chirping technique," DSTO, Tech. Rep., 2014.

[34] L. Zheng and D. Shi, "Maximum amplitude method for estimating compact fractional Fourier domain," *IEEE Signal Processing Letters*, vol. 17, no. 3, 2010.

[35] H. M. Ozaktas *et al.*, "Digital computation of the fractional Fourier transform," *IEEE Trans. on Signal Processing*, vol. 44, no. 9, pp. 2141–2150, 1996.

[36] A. Bultheel and H. E. M. Sulbaran, "Computation of the Fractional Fourier transform," *Applied and Computational Harmonic Analysis*, vol. 16, no. 3, 2004.

[37] H. M.-S. A.Bultheel. (2017). Calculation of the Fractional Fourier Transform, [Online]. Available: http : / / nalag . cs . kuleuven.be/research/software/FRFT/.

[38] K. Kulpa, "The CLEAN type algorithms for radar signal processing," in *Microwaves, Radar and Remote Sensing Symposium*, 2008, pp. 152–157.

[39] M. E. Tipping, "Sparse Bayesian learning and the relevance vector machine," *Journal of machine learning research*, vol. 1, no. Jun, pp. 211–244, 2001.

[40] D. P. Wipf and B. D. Rao, "Sparse Bayesian learning for basis selection," *IEEE Trans. on Signal Processing*, vol. 52, no. 8, pp. 2153–2164, 2004.

[41] D. Shutin and B. H. Fleury, "Sparse variational Bayesian SAGE algorithm with application to the estimation of multipath wireless channels," *IEEE Trans. on Signal Processing*, vol. 59, no. 8, 2011.

[42] H. Rohling, "Radar CFAR thresholding in clutter and multiple target situations," *IEEE Transactions on Aerospace and Electronic Systems*, no. 4, pp. 608–621, 1983.

[43] D. Shutin and N. Schneckenburger, "Joint Detection and Super-Resolution Estimation of Multipath Signal Parameters Using Incremental Automatic Relevance Determination," *arXiv preprint arXiv:1503.01898*, 2015.

[44] B. Nadler and A. Kontorovich, "Model selection for sinusoids in noise: Statistical analysis and a new penalty term," *IEEE Trans. on Signal Processing*, vol. 59, no. 4, 2011.

[45] J. Nocedal and S. Wright, *Numerical optimization*. Springer Science & Business Media, 2006.

[46] T. L. Hansen *et al.*, "Superfast line spectral estimation," *IEEE Transactions on Signal Processing*, vol. 66, no. 10, pp. 2511–2526, 2018.

Alexandra Filip-Dhaubhadel received her Bachelor and Master degrees in Electrical Engineering from Jacobs University Bremen, Germany, in 2011 and 2013, respectively. In September 2013 she joined the Institute of Communications and Navigation at the German Aerospace Center (DLR) as a Research Associate in the Aeronautical Communications group. Her current research focus is on passive multistatic radar systems and the associated radar signal processing techniques.

Dmitriy Shutin received his Master degree in Computer Science in 2000 from Dniepropetrovsk State University, Ukraine, and the Doctoral degree in Electrical Engineering from Graz University of Technology, Graz, Austria, in 2006. During 2001-2006 and 2006-2009, he was a Teaching Assistant and an Assistant Professor, respectively, with the Signal Processing and Speech Communication Laboratory at Graz University of Technology. In 2009 he joined Department of Electrical Engineering at Princeton University, where until 2011 he worked as a Research Associate. In 2011 he joined the Institute of Communications and Navigation, German Aerospace Center, where he is currently a leader of the Swarm Exploration Group. His current research interests include machine learning for signal processing, modeling and estimation of the radio propagation channels, statistical signal processing, and distributed algorithms. Dr. Shutin was a recipient of the Best Student Paper Award at the 2005 IEEE International Conference on Information, Communications and Signal Processing (ICICS). In 2009 he was awarded the Erwin Schroedinger Research Fellowship. Since 2012 till 2014 he acted as selected advisor of German air navigation service provider, within the Navigational System Panel of ICAO. He is Senior Member of IEEE.